11 Supplementary

Supplementary Table 1: **NMR Constraints and Statistics for the final set of structures.**

Non-redundant distance and angle constrains	
Total number of NOE restraints	1565
Short-range NOEs	
Intra-residue (i = j)	421
Sequential (| i - j | = 1)	400
Medium-range NOEs (1 < | i - j | < 5)	169
Long-range NOEs (| i - j | ≥ 5)	569
Torsion angles	134
Hydrogen bond restrains	30
Total number of restricting restraints	1729
Total restricting restraints per restrained residue	18.6
Residual constraint violations	
Distance violations per structure	
0.1 – 0.2 Å	0.23
0.2 – 0.5 Å	0
> 0.5 Å	0
r.m.s. of distance violation per constraint	0.01 Å
Maximum distance violation	0.19 Å
Dihedral angle viol. per structure	
1 – 10 °	2.49
> 10 °	0
r.m.s. of dihedral violations per constraint	0.66°
Maximum dihedral angle viol.	8.50°
Ramachandran plot summary	
Most favoured regions	89.6%
Additionally allowed regions	10.4%
Generously allowed regions	0.0%
Disallowed regions	0.0%
r.m.s.d. to the mean structure	*All / ordered1*
All backbone atoms	1. 0.8 Å
All heavy atoms	1.4 / 1.2 Å
PDB entry	7OMK
BMRB accession code	34630

1Residues with sum of phi and psi order parameters > 1.8

Supplementary Table 2: **Crystallographic statistics PDB ID = 7Z5A**

Crystal structure	mNEIL3(NEI)-DNAhp
Diffraction source	Bessy 14.2
Wavelength (Å)	0.9184
Space group	P 21 21 21
Cell (a, b, c) (Å)	56.16 71.56 94.44
Cell (α, β, γ) (°)	90.0 90.0 90.0
Resolution range (Å)	28.85 - 2.28 (2.341 - 2.28)
Total no. of reflections	212864 (15869)
No. of unique reflections	17642 (1761)
Multiplicity	12.1 (10.8)
Completeness (%)	0.99 (0.96)
Mean $I/\sigma(I)$	9.65 (2.85)
R-merge (%)	16.75 (62.0)
CC1/2	0.992 (0.961)
CC*	0.998 (0.99)
R-work (%)	23.7 (33.0) [24.6]
R-free (%)	26.1 (37.2) [27.6]
Number of non-H atoms	2529
RMSD Bonds (Å)	0.005
RMSD Angles (°)	0.85
Ramachandran (%)	98.06/1.94

Statistics for the highest-resolution shell are shown in parentheses.

R-factors were calculated in the refinement in Phenix Refine (5), those in brackets [R-work/R-free] were calculated during deposition (https://deposit-pdbe.wwpdb.org/)

The rate of formation and stability of abasic site interstrand crosslinks in the DNA duplex

Andrea Huskova [1], Barbora Landova [1], Evzen Boura, Jan Silhan [*]

Institute of Organic Chemistry and Biochemistry of the Czech Academy of Sciences, Flemingovo namesti 2, 166 10 Prague 6, Czech Republic

ARTICLE INFO

ABSTRACT

DNA interstrand crosslinks (ICLs) strands pose an impenetrable barrier for DNA replication. Different ICLs are known to recruit distinct DNA repair pathways. NEIL3 glycosylase has been known to remove an abasic (Ap) site derived DNA crosslink (Ap-ICL). An Ap-ICL forms spontaneously from the Ap site with an adjacent adenine in the opposite strand. Lack of genetic models and a poor understanding of the fate of these lesions leads to many questions about the occurrence and the toxicity of Ap-ICL in cells.

Here, we investigate the circumstances of Ap-ICL formation. With an array of different oligos, we have investigated the rates of formation, the yields, and the stability of Ap-ICL. Our findings point out how different bases in the vicinity of the Ap site change crosslink formation *in vitro*. We reveal that AT-rich rather than GC-rich regions in the surrounding Ap site lead to higher rates of Ap-ICL formation. Overall, our data reveal that Ap-ICL can be formed in virtually any DNA sequence context surrounding a hot spot of a 5′-Ap-dT pair, albeit with significantly different rates and yields. Based on Ap-ICL formation *in vitro,* we attempt to predict the number of Ap-ICLs in the cell.

1. Introduction

Interstrand DNA crosslinks (ICLs) are a type of DNA damage in which opposite DNA strands are covalently linked. ICLs form an impenetrable barrier that prevents DNA replication [1]. Various forms of ICLs that differ both structurally and chemically have been identified [2–5]. To combat the deleterious and toxic consequences of these lesions, distinct DNA repair mechanisms have evolved. At present, two distinct DNA repair processes have been identified. The first repair process is the NEIL3 pathway involving NEIL3 glycosylase, and the second is the Fanconi Anaemia DNA repair pathway (FA pathway) [6,7]. These two pathways are intrinsically linked to DNA replication and complement each other in the repair of ICLs. The NEIL3 pathway has been linked to an early stage of replication coupled repair when replication forks stall on the crosslink and is known for the removal of abasic site ICLs (Ap-ICLs) [4,8]. Additionally, NEIL3 is also involved in the recognition and excision of psoralen-induced ICLs. The same ability has also another glycosylase, NEIL1. Importantly, the excision activity of these glycosylases doesn't generate double-strand breaks [9]. The later recruited FA pathway recognises and repairs crosslinks arising from small aldehydes such as acetaldehyde derived crosslinks. It has been identified and it is known for its ability to repair DNA crosslinks generated from exogenous crosslinking compounds, used as chemotherapeutics or in warfare (*e.g.* cis-platin and nitrogen mustard) [10–12].

An abasic site (apurinic/apyrimidinic), or an Ap site, can be generated spontaneously in large quantities, as it was estimated that 10,000 Ap sites form per cell every day [13,14]. This astronomical number is increased even further, mainly by some DNA glycosylases that remove damaged bases from the genome [15]. One of the most well-known is Uracil DNA glycosylase, an important enzyme not only in base excision repair but also in somatic hypermutation during the diversification of antibodies [16–19]. It removes uracil, generated either by spontaneously or enzymatic deamination of cytosine. The Ap site undergoes spontaneous or enzymatic cleavage. The Ap endonucleases cleave the phosphodiester bond of the Ap site while producing a nick with 3′-deoxyribose-5′-phosphate and a single-strand DNA (ssDNA) break [20,21]. Two groups of Ap lyases cleave the Ap site either *via* β-elimination generating an unsaturated 3′-aldehyde or through the β-δ

---

elimination to yield 3′-phosphate [22,23]. The Ap site also undergoes spontaneous breakage with a half-life of 8 days, and the rate can be enhanced by basic hydrolysis catalysed by amines or an increase of pH. First, the Ap site undergoes β-elimination followed by δ-elimination with 3′-phosphate as the final endproduct [24,25]. These toxic 3′-lesions block ligation and replication and are generally repaired by specific 3′-phosphates, such as PNK or Ap exonucleases [26–29]. Finally, the generated ssDNA break with 3′-OH is repaired by a DNA polymerase and ligase [25,30,31]. A nucleophilic attack of the Ap site may form a DNA interstrand crosslink or a DNA-protein crosslink [4,32].

From a chemical point of view, an Ap site undergoes structural changes, such as mutarotation and spontaneous decomposition [33]. Spontaneous base loss is caused by hydrolysis where the C1 of deoxyribose is attacked by a water molecule from the opposite side of the N-glycosidic bond [30]. This reaction leads to the formation of an Ap site with an alpha-OH group at C1. Further on the Ap site, it undergoes mutarotation until the thermodynamic equilibrium is reached [33,34]. Interestingly, this process reaches equilibrium when only 1% of the ribose ring opens to its aldehyde form [33,35]. Aldehydes are reactive groups that readily interact with amines, forming a relatively stable covalent imine commonly known as a Schiff base [36–38].

Very early on, it was suggested that the Ap site can generate ICL in double-stranded DNA [39,40]. This was later confirmed and further investigated in several publications [41–43]. Most of these experiments were carried out at relatively low pH, somewhat harsh and non-physiological conditions. Nonetheless, one rough estimate at pH = 6.8 in T7 phage DNA was that 1 crosslink is formed per 140 Ap sites [40]. Eventually, the nature of the chemical agent responsible for

crosslink formation on the Ap site was found to be the aldehyde group, and the optimum for Ap-ICL formation is in the low pH region [44].

Successfully reconstituted Ap-ICL at a specific site *in vitro* was accomplished for the Ap site crosslinking with guanine in an opposite DNA strand within the 5′-dC-Ap sequence [4]. These crosslinks were formed under relatively acidic conditions (pH = 5) and stabilized by the reduction with sodium cyanoborohydride (NaBH₃CN) and characterized by mass spectroscopy. Shortly thereafter, another Ap-ICL was discovered where the Ap site linking with opposing adenine downstream of the Ap site, and therefore a different sequence context (5′-ApT) was confirmed. This Ap-ICL was shown to be stable, and it formed under physiological conditions [46]. A subsequent NMR study confirmed that one of the Ap-ICLs generated between ApT:A is attached with the N6-amino group of the dA from the opposite strand [47]. In this study, Ap-ICL was extracted from the duplex by enzymatic digestion and analysed by NMR. The presence of different sugar moiety isomers was found in equilibrium. The latest NMR study reveals that the structure of Ap-ICL has the Ap site's ribose ring closed in its furanose form [45]. In this work, the DNA contains a 5′-dC-Ap-dT sequence (Fig. 1).

These studies have sparked questions regarding the repair of these Ap-ICLs in the cell. The first repair that was discovered is linked to replication and is orchestrated by the DNA glycosylase NEIL3 [7]. Subsequently, it was demonstrated that this enzyme requires a replication fork with a specific orientation of the Ap part of the lesion to be catalytically efficient. Furthermore, NEIL3 is recruited to the ICL by TRAIP1 dependent ubiquitylation of DNA helicase which initiates the ICL repair [8]. Finally, it has been described that particular orientation of the Ap-ICL site within the DNA fork is necessary for sufficient removal
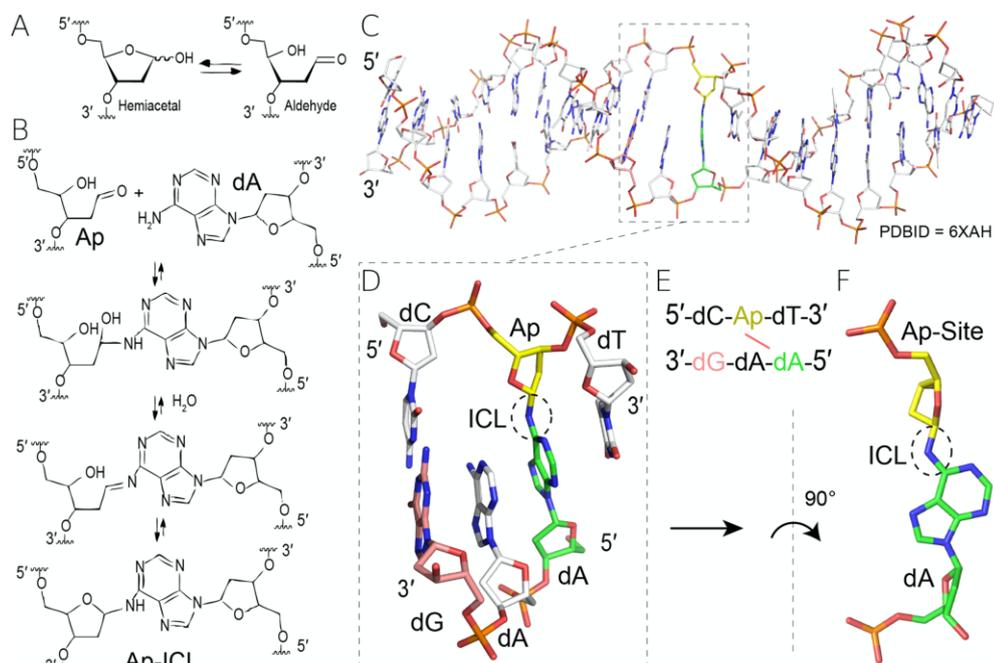

Fig. 1. Structure, sequence and formation of the Ap-ICL.A) The Ap site in an open and closed form, B) schematics of formation of Ap-ICL. C) The NMR model of the structure of Ap-ICL. D). An enlarged side view of the Ap-ICL within the duplex DNA with orphaned bases (Ap site in yellow, dG which is known to also form Ap-ICL in pink, and crosslinked adenine in green), E) the DNA sequence schematics in the vicinity of Ap-ICL in this NMR structure, and F) top view of the Ap-ICL crosslink (C-F) [45].(For interpretation of the references to colour in this figure, the reader is referred to the web version of this article.)

of the Ap-ICL [48]. The knowledge regarding the feasibility and prevalence of the Ap-ICL, however, remains elusive. Moreover, the circumstances such as the local sequence leading to formations and its kinetics are also only fragmental.

Here, we aim to reveal a sequence of contexts and conditions leading to the formation of the Ap-ICL *in vitro* and to predict the relevance, frequency and feasibility of Ap-ICL formation *in vivo*. With this goal in mind, we designed a panel of DNA oligonucleotides to study the rate of formation of Ap-ICL *in vitro* with regard to the sequence context. Our data reveal that individual changes in nucleobases surrounding Ap-ICLs influence the rate of formation of the Ap-site, but only to a certain extent. Significant changes in formation rates have been observed for Ap-ICLs generated within the duplex with AT-rich regions surrounding the crosslink lesion. We then followed the stability of the purified Ap-ICLs, and from our biochemical experiments regarding the formation of Ap-ICLs, we have estimated a theoretical number of Ap-ICLs formed in a living cell.

2. Materials and methods

2.1. Oligonucleotides for preparation of DNA containing native Ap site

All synthetic DNA oligonucleotides were acquired from (Sigma-Aldrich). Oligonucleotides for the preparation of native Ap sites were ordered with deoxy-uracil and were labelled with HEX (Table 1).

2.2. DNA crosslink formation

The reaction buffer for crosslinking reactions was optimized. The final reaction buffer was composed of 20 mM HEPES, pH = 6.5, 140 mM NaCl, 0.5 mM TCEP, and 5% glycerol. Comparative crosslinking experiments were carried out at Tris-HCl pH = 7.4, 140 mM NaCl and 5% glycerol to outline the similarity of results under physiological conditions (Supplementary Fig. S4). We mixed labelled DNA oligonucleotides with non-labelled complementary oligonucleotides 1:1 in an optimized buffer to the final DNA concentration of 2.5 µM. The DNA reaction mixture (50 µl) was annealed using Biometra Tprofessional Thermocycler by heating to 95 °C and then cooling to room temperature using the slowest ramp. For the Ap site creation, 0.5 U uracil-DNA glycosylase

(UDG) (New England Biolabs) per one sequence reaction was added and kept 5 min at room temperature. Afterwards, UDG was inactivated with another round of an annealing cycle. The annealed DNA reaction mixture containing the Ap site was incubated for the duration of the experiment at 37 °C. At given time points, 1 ul of the crosslinking reaction was taken and mixed with 9 ul of formamide to stop the reaction. The stopped reaction was separated on a 20% denaturing polyacrylamide gel (1 x TBE, 7 M Urea 20% polyacrylamide: bisacrylamide 19:1) and visualized using a 532 nm laser and using a Cy3 570BP20 filter on an Amersham Typhoon Biomolecular Imager (GE Healthcare). The progress of the crosslinking reaction was quantified using a commercial ImageQuant TL. All bands in the individual lanes (substrate, product and intermediates) were densitometrically quantified to determine the percentage of the crosslink formed, the methodology was described previously in detail [49]. Control reaction with thymine in place of uracil to prevent Ap-ICL reaction was carried out with and without UDG, this control aimed to demonstrate the specificity of crosslinking at Ap site (Supplementary Fig. S2).

2.3. Isolation of crosslinked DNA from polyacrylamide gel for further reactions

Ap-ICL crosslink was purified from the PAGE gel using the modified band excision method from the gel [50]. The sample of crosslinked DNA was run on a 20% denaturing polyacrylamide gel. Bands were visualized using HeroLab UVT-20 S/M/L, and a band of crosslinked DNA was cut out, chopped and transferred to a tube with 200 µl of elution buffer (20 mM Tris, pH 7.4, 140 mM NaCl, 0.5 mM TCEP, 5% glycerol). The tube was left on a rotating wheel at 8 °C overnight. The sample was then centrifuged at 800 g for 1 min. The remaining buffer was recovered and purified using Cytiva MicroSpin™ G-25 Columns against the elution buffer to remove excess urea. The final sample of purified Ap-ICL DNA was run on 20% denaturing polyacrylamide gel to verify its purity.

2.4. Analysis of degradation of crosslinked DNA

The stability of crosslinked DNA was assessed at 37 °C in 20 mM Tris, pH 7.4, 140 mM NaCl, 0.5 mM TCEP, 5% glycerol. At given time points, typically 1 day, 2 µl of a solution of crosslinked DNA was taken, 8 µl of

Table 1

DNA oligonucleotide sequences. Sequences of dsDNA oligonucleotides, and their names used in this study. Ap site is generated from uracil (U) on the position 2 and Ap-ICL forms with adenine on the position 6, the reaction confirming the specificity of Ap-ICL crosslinking reaction is shown in Supplementary Fig. S3.

4G	5'[HEX]-GTCGATGAAC$_1$**U$_2$**T$_3$AGACAGCT 3'-CAGCTACTT**G$_4$**A$_5$**A$_6$**TCTGTCGA	4I	5'[HEX]-GTCGATGAAC$_1$**U$_2$**T$_3$AGACAGCT 3'-CAGCTACTT**I$_4$**A$_5$**A$_6$**TCTGTCGA
4C	5'[HEX]-GTCGATGAAC$_1$**U$_2$**T$_3$AGACAGCT 3'-CAGCTACTT**C$_4$**A$_5$**A$_6$**TCTGTCGA	6I	5'[HEX]-GTCGATGAAC$_1$**U$_2$**T$_3$AGACAGCT 3'-CAGCTACTTG$_4$A$_5$**I$_6$**TCTGTCGA
4T	5'[HEX]-GTCGATGAAC$_1$**U$_2$**T$_3$AGACAGCT 3'-CAGCTACTT**T$_4$**A$_5$**A$_6$**TCTGTCGA		
4(5)A	5'[HEX]-GTCGATGAAC$_1$**U$_2$**T$_3$AGACAGCT 3'-CAGCTACTT**A$_4$**A$_5$**A$_6$**TCTGTCGA	TT	5'[HEX]-GTCAGATC**AAA**$_1$**U$_2$**T$_3$**AA**ACCTG 3'-CAGTCTAG**TTT**$_4$G$_5$**A$_6$TT**TGGAC
5G	5'[HEX]-GTCGATGAAC$_1$**U$_2$**T$_3$AGACAGCT 3'-CAGCTACTTA$_4$**G$_5$**A$_6$**TCTGTCGA	TC	5'[HEX]-GTCAGATC**AAG**$_1$**U$_2$**T$_3$**AA**ACCTG 3'-CAGTCTAG**TTC**$_4$G$_5$**A$_6$TT**TGGAC
5C	5'[HEX]-GTCGATGAAC$_1$**U$_2$**T$_3$AGACAGCT 3'-CAGCTACTTA$_4$**C$_5$**A$_6$**TCTGTCGA	GT	5'[HEX]-GTCAGATC**CCA**$_1$**U$_2$**T$_3$**CC**ACCTG 3'-CAGTCTAG**GGT**$_4$G$_5$A$_6$**GG**TGGAC
5T	5'[HEX]-GTCGATGAAC$_1$**U$_2$**T$_3$AGACAGCT 3'-CAGCTACTTA$_4$**T$_5$**A$_6$**TCTGTCGA	GC	5'[HEX]-GTCAGATC**CCG**$_1$**U$_2$**T$_3$**CC**ACCTG 3'-CAGTCTAG**GGC**$_4$G$_5$A$_6$**GG**TGGAC

formamide was added, and the sample was frozen at −80 °C to terminate the degradation. After that, all samples were resolved on 20% denaturing polyacrylamide gel to validate the progress of degradation. The gel was scanned using a laser at 532 nm and a Cy3 570BP20 filter on the Amersham Typhoon Biomolecular Imager (GE Healthcare). The image was analyzed using the commercial ImageQuant TL. Lines were selected manually, and the background subtraction was performed using the rolling ball method. Bands with constant dimensions encompassing crosslinked DNA and degradation products were selected manually. For every line, the percentage of degradation of crosslinked DNA was calculated based on the ratio of the remaining crosslinked DNA and the degradation product.

3. Results

3.1. Design of the DNA substrates

Uracil, and thus the Ap site, was situated in the middle of the oligonucleotide duplex. All residues in the vicinity were named

accordingly (Fig. 2A), and the position of the Ap site was numbered 2. The base to which the majority of crosslinks is formed was fixed to be adenine at position 6 [36]. Therefore, in our experimental setup, positions 2 and 6 were constant as there were involved in the Ap-ICL formation with the exception of a control experiment validating the preferential formation of these sites. Only natural DNA nucleobases were altered in other positions to obtain all possible combinations in the vicinity of the Ap site. Position 5 is opposite to the Ap site lesion. Because positions 1 and 4 were intrinsically linked by complementarity, thereafter the experiments were focused on positions 4 and 5. Subsequently, a wider area of the Ap site was investigated with the specific goal of comparing the AT-rich and GC-rich regions (Fig. 3).

3.2. Generation of the Ap site and crosslink formation

Purchased synthetic DNA oligonucleotides contained deoxyuridine and were labelled with 5′ fluorescent dye (HEX, 6-hexachloro-fluorescein). Uracils were introduced to easily generate a native Ap site. First, the oligos were annealed with a complementary DNA strand and
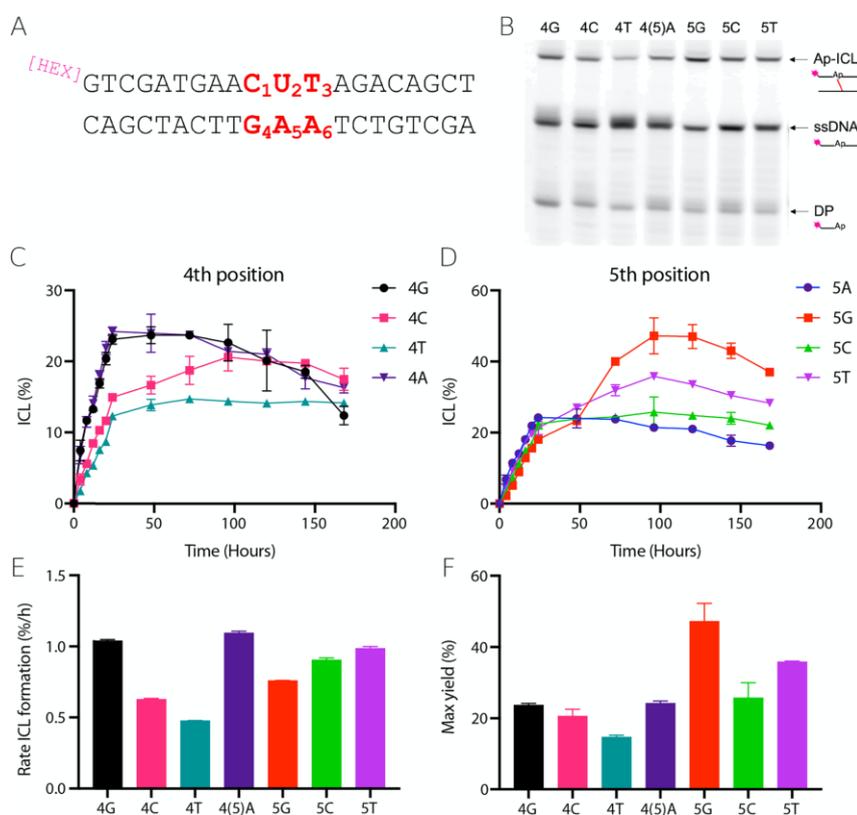

Fig. 2. Reaction kinetics of the Ap site DNA when varying bases at positions 4 and 5, respectively.*(A) Schematic design of the DNA duplex containing the Ap site and nomenclature of different positions. Position 2 is where the Ap site is formed by reaction with UDG, and ICL is formed between positions 2 and 6. Reactions were initiated by the formation of the Ap site by UDG and kept in dark at 37 °C (B) Reactions in each timepoint were stopped (here 24 h) and immediately resolved on 20% denaturing PAGE gel, ssDNA marks single-stranded DNA and DP donates degradation product. The gels were evaluated and the proportion of Ap-ICL formed from DNA oligos with different nucleobase in position 4(C) or position 5(D) were plotted in the graph. The initial rates of Ap-ICL formation (E) and the maximum yield (F) of Ap-ICL we plotted as bar charts. Error bars represent SEM from three independent repeats. Comparative gel at Tris-HCl pH = 7.4, 140 mM NaCl shown in the Supplementary Fig. S4.*
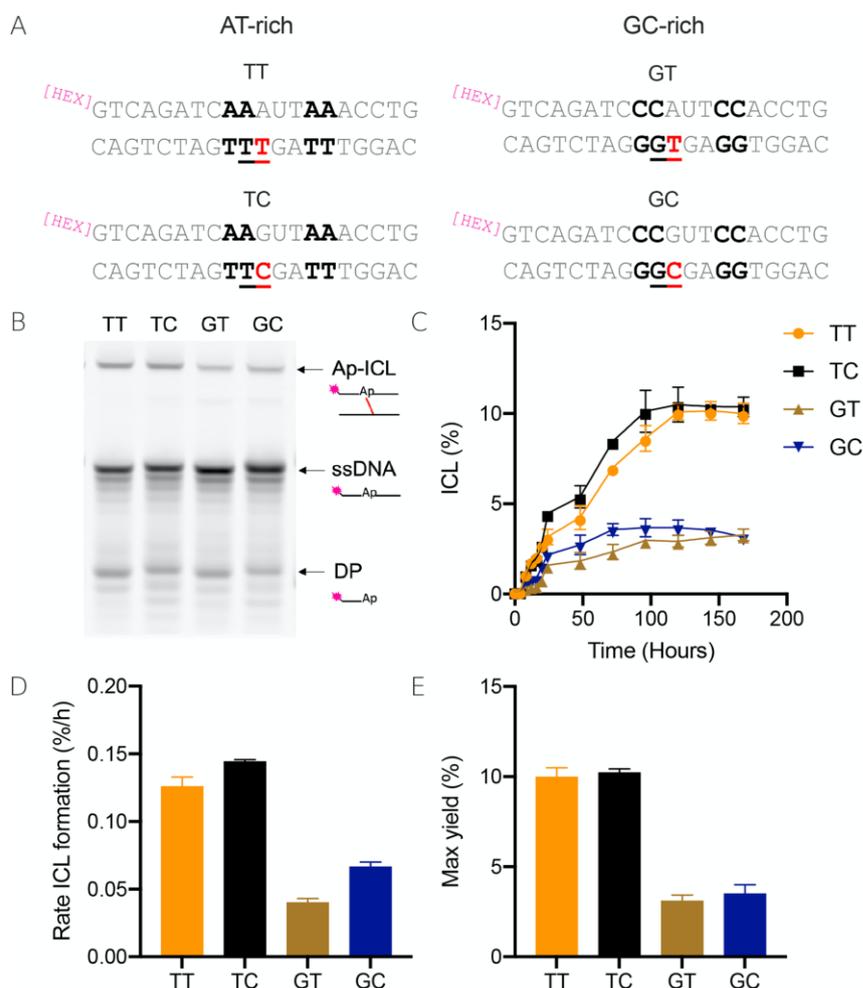
Fig. 3. Formation of Ap-ICL in DNA duplexes with AT-rich or GC-rich regions. *(A) Schematics of DNA duplexes containing i) AT-rich regions (left) or ii) GC-rich regions (right), in the vicinity of the Ap site. AT-rich sequences where thymine and cytosine are interchanged in the 4th position are named TT or TC; similarly, GC-rich sequences with bases in the 4th position are named GT or GC. (B) Reactions were resolved on 20% denaturing PAGE gel, ssDNA marks single-stranded DNA and DP donates degradation product. (C) Reaction kinetics of Ap-ICL formation from DNA oligos with AT-rich or GC-rich regions. The rate of ICL formation (D) and the maximum yield (E) were plotted for all four sequences. Error bars represent SEM from four independent repeats.*

incubated with an UDG [51,52]. The minimal amount of this enzyme was estimated by its titration into the reaction mixture. The presence of the generated Ap site was monitored on the PAGE gel after its sufficient hydrolysis by NaOH at an elevated temperature (Supplementary Fig. S1). Typically, a 5 min incubation with UDG was sufficient for a total conversion of the uracil to the Ap site.

The crosslinking reaction was allowed to proceed in a dark incubator at 37 °C. Aliquots were taken at different time points to monitor the time course. The fluorescently labelled samples were analyzed on denaturing PAGE gels, imaged, quantified and the percentage of generated crosslink was plotted in a graph. Initial rates were calculated as a linear fit to the

data and maximum yields of Ap-ICL were determined as the maximum measured value.

3.3. The opposite nucleotide to the Ap site influences the rate of formation of Ap-ICL

The chemical nature of the DNA is as such that Ap sites can be generated spontaneously at any given DNA context [30]. In our first set of experiments, the single base opposing the Ap site was varied whilst the sequence of the entire remaining DNA duplexed was identical. In this setup, all four bases were tested on this position that we named the 5th

position (Fig. 2A), The rate of formation of Ap-ICLs were followed so as the maximum yields. The data were plotted in the graph and to bar charts. The observed rates were 1.1%/h for 5 A, 0.76%/h for 5 G, 0.91%/h for 5 C and 0.99%/h for 5 T (we took the liberty to express the rates in the percentage of original Ap sites converted in one hour to Ap-ICL). The maximum yield for all these oligos was 24.25% for 5 A, 47.2% for 5 G, 25.8% for 5 C and 35.9% for 5 T of the total DNA (For further rates please refer to Supplementary Tables ST1 – ST3). Later, with an increasing amount of degradation product, the amount of Ap-ICL started to decline. There were significant differences in the rate of formation as shown in the graph. Overall, these changes were relatively small and regardless of the nucleobase present opposite to the Ap site the Ap-ICL formed to a similar extent (Fig. 2).

3.4. Varying base-pair adjacent to Ap site on its 5′ end

Similar to the variation of the bases opposite to the AP site, the adjacent base-pair occupying positions 1 and 4 were varied. All four base pair combinations were tested for these positions and DNA oligonucleotides were named 4 G, 4 T, 4 C, and 4(5)A. Sequences 4 A and 5 A are identically co-named 4(5)A as 4 A was kept constant at 5th position and *vice-versa* with sequence 5 A. Yet again, significant differences in the formation of the Ap-site crosslink were observed. Surprisingly enough, the differences in rates of formation were not extraordinary, but the Ap-ICL was yet again formed in all possible base combinations. Overall, the rates vary approximately 2-fold (Supplementary Table ST1). The maximum yield varies slightly, and it was reached at different time-points (Fig. 2 & ST1). The initial rate was the lowest for both pyrimidine bases. Both thymine and cytosine containing duplexes reached their maximum yield of crosslinks later but the percentages were not dissimilar with the remaining two bases at this position. Once again the amount of crosslinks starts to decline due to the irreversible decomposition to smaller degradation products (Fig. 2). To confirm published work and demonstrate the specificity of Ap-ICL forming from Ap with adenine residues, two control experiments were carried out. For sequence 4 G, hypoxanthine was placed at positions 4 and 6. No visible Ap-G crosslink was formed when adenine at position 6 was mutated to hypoxanthine. In contrast, when hypoxanthine was placed at position 4, however, Ap-A crosslink was formed as readily as when guanine was present (Fig. SI 3).

3.5. AT-rich regions facilitate Ap-ICL formation

Investigating the sequence surrounding the Ap site has revealed the differences in the rate of Ap-ICL formation, although a more complete picture requires investigation of further sequence variation that may influence the rigidity of the entire region encompassing the Ap site. We modified the sequence in the wider surrounding of the Ap site by a set of two AT or GC pairs from both sites (Fig. 3A). We set out to determine how AT-rich and GC-rich sequences influence the rate of formation of Ap-ICL. These sequences were tested in non-identical duplicates for which the base at 4th position contained either cytosine or thymine and the oligos were named accordingly (TT, TC, GT, GC), *e.g.* TC is an AT-rich oligonucleotide with C at 4th position (Fig. 3A). These bases were chosen to extend the AT-rich or GC-rich part around the Ap-site. The reaction set-up was identical as above, where reaction progress was monitored on a denaturing PAGE gel. The amount of formed Ap-ICL was apparent from the gel figures (Fig. 3B). Next, the gels were evaluated, and initial reaction rates were determined from the slopes of the data points.

When AT- and GC-rich regions were swapped, we observed significant differences in the rate of formation (Fig. 3C). The effect of the cytosine or thymine base at the 4th position on the rate of the reaction is rather small and the rates for oligos containing cytosine were faster than those with thymine. This was observed for both AT-rich and GC-rich DNA duplexes, and this trend was consistent in experiments shown in

Fig. 2 and Fig. 3 confirming the robustness of our approach. Finally, the rate of formation for the AT-rich sequence with a cytosine at 4th position (TC) had a nearly 4 times higher rate of formation than the one with GC-rich sequence with thymine at 4th position (GT). This trend was observed for both pairs of sequences (TC > TT >>> GC > GT), and it was also reflected in a maximum yield reaching an approximate 2.5-fold difference (Fig. 3E).

3.6. Stability of Ap-ICL

Finally, the stability of Ap-ICL was tested to determine how persistent the crosslink could be at physiological conditions and without the intervention of other proteins and enzymes. The Ap-ICLs were purified by isolation from the gel. Large volumes of the crosslinking reactions stopped approximately at the timepoint for the maximum yield of the Ap-ICL. After their isolation, the pure Ap-ICLs were buffer-exchanged into a physiological buffer and subjected to their spontaneous decomposition. Our initial experiments as well as published literature have suggested that the decomposition of Ap-ICL is a lengthy process [53]. Therefore, the subsamples were taken in 24 h intervals, and after two weeks, all reaction time points were resolved on denaturing PAGE gels (Fig. 4 A). The proportions of degrading Ap-ICL were plotted as a function of time, the initial reaction rates of their decomposition were fitted with single exponential decay and plotted into a bar chart (Fig. 4B & 4 C). The ICL band disintegrated into a band the size of the original substrate. With a delay, more products appeared, with the nature of these substrates arising from the spontaneous hydrolysis of the Ap site. Sequences with AT- and GC-rich regions were used in this experiment, and all reactions had a similar rate of decomposition, except for an AT-rich sequence with a T at the 4th position (TT) that decomposed at a slightly slower rate. Less than 1/5 of the initial material was decomposed in the first 10 days (Fig. 4).

4. Discussion

The first studies of specific Ap-ICL outlined two possible ways by which the Ap-ICL can form [2,37]. They demonstrated that within a duplex within this exemplary sequence 5′-dC-Ap-dT, Ap-ICL can be formed by crosslinking Ap with guanine or adenine in the opposite DNA strand. The latter study showed that an Ap-G crosslink is not stable unless reduced with NaBH$_3$CN. This is presumably due to its sterically unfavourable arrangement, and the crosslink reverted back to the Ap site. Importantly, and perhaps coincidentally, the identical sequence motif was used to determine the NMR structure of Ap-ICL within the DNA duplex. In this study, only one type of crosslink was observed, making a 5′Ap-dT "hotspot" of Ap site crosslink formation *in vivo* (Fig. 1) [36]. Recently, another Ap-ICL where Ap site linking amino group of cytosine from opposite DNA strand (Ap-C) was observed. This Ap-ICL was preferentially formed within where C was mispaired with A. This crosslink was only formed at quite acidic conditions pH = 5 and was shown not to form under physiological conditions in nonmispaired oligonucleotide [54].

In this manuscript, we focused on Ap-ICL formed within this 5′-Ap-dT "hot-spot". We have a synthesized and annealed panel of DNA oligonucleotides with different DNA sequences surrounding the Ap site. The entire study used this non-enzymatic Ap-ICL formation, and by measuring its kinetics, we revealed sequence circumstances and influences leading to the formation of ICLs. To investigate the generation of the Ap-ICL, uracil was converted to the Ap site by an enzymatic reaction with UDG. We then set up the reactions to measure the rates of ICL formation for individual oligonucleotides with different sequences. Reactions were terminated at different time points, resolved on PAGE gels and the fractions of crosslinks formed were plotted against time. This allowed us to follow the kinetics of ICL formation. Our data has revealed that different nucleotides surrounding the Ap site affected the rate of the Ap-ICL formation. Although the rates differed to an extent,
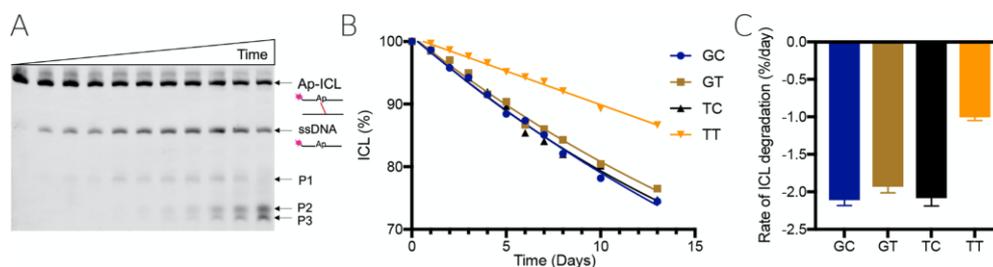
Fig. 4. Stability and degradation of Ap-ICL with AT-rich or GC-rich regions. *Gel purified Ap-ICLs from DNA oligos with AT-rich or GC-rich regions flanking the Ap site were subjected to spontaneous degradation at physiological conditions. (A) An illustrative 20% denaturing PAGE gel of Ap-ICL degradation in time is shown, where P1, P2 and P3 are products of degradation. HEX-labelled fluorescent imaging. (B) Degradation of Ap-ICL was plotted over time and fitted with exponential decay (C) The rate of Ap-ICL degradation was plotted and is represented as a bar chart. The half-lives for GC, GT, TC and TT were 28.8; 31.7; 29.3 and 60.6 days.*

what we found most striking was that the Ap-ICLs form consistently within all of these sequences and that the resulting crosslinks were very stable with a half-life longer than 30 days. This is in agreement with the literature where different Ap-ICL were already been reported to be relatively stable [47,53–55].

The data show that the rate of formation of the Ap-ICLs is only slightly affected by different single nucleotide or one base pair substitutions in the vicinity of the Ap site. The maximum yield of Ap-ICLs for all of these sequences was roughly 15%. Meaning that on average 15% of Ap sites are converted into Ap-ICLs. On the other hand, the formation of ICLs is significantly affected by the presence of AT-rich or GC-rich regions flanking the Ap site. In the case of AT-rich sequences, we observed significantly higher rates of formation. We speculate that this may be because AT-rich regions have a lower melting temperature and thus allow for "DNA breathing". We predict that weaker base-pairing, in turn, would allow for crosslinking reactions to proceed with less difficulty and faster. Although our study is focused purely on the *in vitro*, non-enzymatic formation of Ap-ICLs, the study aimed to broaden understanding of which circumstances and how often the crosslinks can form *in vivo*. Below, we attempt to make a rough estimate on the number of Ap-ICLs in one human cell, as our work shed light on a rough number of Ap-ICLs formed per 100 Ap sites.

Spontaneous deamination and depurination generate 10,000 Ap/sites/day in a cell [13,14]. In addition to this, the DNA damage and action Ap site generation by various DNA glycosylases further increase this number [30]. To accurately count this number can be challenging. Our rough estimate disregards that DNA repair enzymes are present, and they eliminate the majority of Ap sites. Then, observable Ap sites at any given moment may only represent 0.25–4% of the sites that would form the Ap-ICL during the day. We may predict that the majority of these Ap sites are repaired or protected by the formation of DNA protein crosslinks, and therefore only a small proportion of Ap sites are present [53, 56–58]. In recent work, a relative number of Ap-sites were estimated and compared against the knockdown of human Ap endonuclease APEX1. It has been observed that an extra 77% more Ap sites were present in the knockdown, while 90% of the enzyme was removed [59]. It is difficult to estimate the original numbers of Ap sites from this relative comparison, but these numbers suggest that significant numbers still persist in the genome.

With DNA fibre analysis, it was predicted that the number of Ap sites to be more than 35,000 Ap sites in one human cell [56]. On the other hand, further methods for determining the presence of Ap sites have been developed. A mass spectroscopy method using a chemical O-(pyridine-3-yl-methyl) hydroxylamine (PMOA) is reportedly a very sensitive technique for the detection of Ap sites directly within the duplex [60]. This technique is quantitative and allows for the detection of up to 2 Ap sites in 10^8 nt. With such sensitivity, a rough number of the

steady-state Ap sites detected by this method is 2 Ap sites per 10^7 nt [61]. Considering that the human genome has 3.2×10^9 nt and is diploid, then one human cell would have only 160 Ap sites. It is noteworthy, that experiments using aldehyde reactive probes might be biased as the probe may react with other aldehydes in the DNA. The Ap site undergoes a mutarotation as do other sugar moieties, and generally, only less than 1% of the sugars are in open aldehyde form [33,35]. Therefore, the rate of derivatization of the Ap site with an aldehyde reactive probe will be determined by the ring-opening reaction of the ribose into the aldehyde form. The rate of ring-opening can be noticed in mass spectroscopy studies where PMOA reagent was used. Here, almost the full conversion of small DNA oligonucleotide containing Ap site to a PMOA adduct was shown on HPLC chromatograms and confirmed by mass spectroscopy [62]. Additionally, a biochemical study with an aldehyde reactive probe conjugated with biotin showed that the majority of Ap sites were conjugated with the probe if sufficient time and reagents were in supply [63]. Both studies with PMOA, including one with mammalian samples, used excessive amounts of PMOA allowing first-order kinetics where ring-opening of Ap site is a rate-limiting reaction. Thereafter, we believe that HPLC-MS detection of conjugated Ap-sites is specific and validated by the MS method and might be the most accurate. This leads to a steady-state value of only about 100–200 Ap sites present in the genome. Moreover, product inhibited bifunctional glycosylases may bind and crosslink the Ap-sites [32,64,65]. Other DNA repair enzymes and DNA binding proteins interacting with Ap sites could impede the Ap-ICL formation thus protecting the genome integrity [57,66,67]. Additionally, it has been also shown that Ap-ICL crosslink can be reverted beside the repair by NEIL3 glycosylase [7, 53]. On the other hand, human Ap endonuclease and exonuclease APEX1 was shown to cleave the Ap-ICL using its exonuclease activity on degraded Ap-G crosslink. These protective processes could explain the relatively low number of Ap sites detected using PMOA and mass spectroscopy. Based on the aforementioned predictions and our data, we estimate the amount of Ap-ICL crosslink to be 1–5 Ap-ICLs present or formed in any human cell.

Author contribution

Acknowledgements

project was also supported by the Academy of Sciences Czech Republic (RVO: 61388963). We cordially acknowledge Edward Curtis and Tamara Jenkins for the critical reading and proofreading of the manuscript.

Appendix A. Supporting information

Supplementary data associated with this article can be found in the online version at doi:10.1016/j.dnarep.2022.103300.

References

[1] J. Zhang, J.C. Walter, Mechanism and regulation of incisions during DNA interstrand cross-link repair, DNA Repair 19 (2014) 135–142, https://doi.org/10.1016/j.dnarep.2014.03.018 ((Amst)).

[2] F. Coste, J.-M. Malinge, L. Serre, W. Shepard, M. Roth, M. Leng, C. Zelwer, Crystal structure of a double-stranded DNA decamer containing a cisplatin interstrand cross-link adduct, Nucleic Acids Res. 27 (1999) 1837–1846.

[3] D.M. Noll, T. McGregor Mason, P.S. Miller, Formation and repair of interstrand cross-links in DNA, Chem. Rev. 106 (2006) 277–301, https://doi.org/10.1021/cr040478b.

[4] K.M. Johnson, N.E. Price, J. Wang, M.I. Fekry, S. Dutta, D.R. Seiner, Y. Wang, K.S. Gates, On the formation and properties of interstrand DNA-DNA cross-links forged by reaction of an abasic site with the opposing guanine residue of 5′-CAp sequences in duplex DNA, J. Am. Chem. Soc. 135 (2013) 1015–1025, https://doi.org/10.1021/ja308119q.

[5] J. Nakamura, M. Nakamura, DNA-protein crosslink formation by endogenous aldehydes and AP sites, DNA Repair 88 (2020), 102806, https://doi.org/10.1016/j.dnarep.2020.102806 ((Amst)).

[6] M. Räschle, P. Knipsheer, M. Enoiu, T. Angelov, J. Sun, J.D. Griffith, T.E. Ellenberger, O.D. Schärer, J.C. Walter, Mechanism of replication-coupled DNA interstrand crosslink repair, Cell 134 (2008) 969–980, https://doi.org/10.1016/j.cell.2008.08.030.

[7] D.R. Semlow, J. Zhang, M. Budzowska, A.C. Drohat, J.C. Walter, Replication-dependent unhooking of DNA interstrand cross-links by the NEIL3 Glycosylase, e14, Cell 167 (2016) 498–511, https://doi.org/10.1016/j.cell.2016.09.008.

[8] R.A. Wu, D.R. Semlow, A.N. Kamimae-Lanning, O.V. Kochenova, G. Chistol, M.R.G. Hodskinson, R. Amunugama, J.L. Sparks, M. Wang, L. Deng, C.A. Mimoso, E. Low, K.J. Patel, J.C. Walter, TRAIP is a master regulator of DNA interstrand crosslink repair, Nature 567 (2019) 267–272, https://doi.org/10.1038/s41586-019-1002-0.

[9] P.R. Martin, S. Couvé, C. Zutterling, M.S. Albelazi, R. Groisman, B.T. Matkarimov, J.L. Parsons, R.H. Elder, M.K. Saparbaev, The human DNA glycosylases NEIL1 and NEIL3 excise psoralen-induced DNA-DNA cross-links in a four-stranded DNA structure, Sci. Rep. 7 (2017) 1–13, https://doi.org/10.1038/s41598-017-17693-4.

[10] P. Knipscheer, M. Räschle, A. Smogorzewska, M. Enoiu, T.V. Ho, O.D. Schärer, S.J. Elledge, J.C. Walter, The fanconi anemia pathway promotes replication-dependent DNA interstrand cross-link repair, Science 326 (2009) 1698–1701, https://doi.org/10.1126/science.1182372.

[11] M.R.G. Hodskinson, J. Silhan, G.P. Crossan, J.I. Garaycoechea, S. Mukherjee, C.M. Johnson, O.D. Schärer, K.J. Patel, Mouse SLX4 is a tumor suppressor that stimulates the activity of the nuclease XPF-ERCC1 in DNA crosslink repair, Mol. Cell. 54 (2014) 472–484, https://doi.org/10.1016/j.molcel.2014.03.014.

[12] M.R.G. Hodskinson, A. Bolner, K. Sato, A.N. Kamimae-Lanning, K. Rooijers, M. Witte, M. Mahesh, J. Silhan, M. Petek, D.M. Williams, J. Kind, J.W. Chin, K.J. Patel, P. Knipscheer, Alcohol-derived DNA crosslinks are repaired by two distinct mechanisms, Nature 579 (2020) 603–608, https://doi.org/10.1038/s41586-020-2059-5.

[13] T. Lindahl, B. Nyberg, Rate of depurination of native deoxyribonucleic acid, Biochemistry. 11 (1972) 3610–3618. ⟨http://www.ncbi.nlm.nih.gov/pubmed/4626532⟩.

[14] T. Lindahl, a Andersson, Rate of chain breakage at apurinic sites in double-stranded deoxyribonucleic acid, Biochemistry. 11 (1972) 3618–3623. ⟨http://www.ncbi.nlm.nih.gov/pubmed/4559796⟩.

[15] D. Svilar, E.M. Goellner, K.H. Almeida, R.W. Sobol, Base excision repair and lesion-dependent subpathways, Antioxid. Redox Signal. 14 (2011) 2491–2507.

[16] C.D. Mol, A.S. Arvai, R.J. Sanderson, G. Slupphaug, B. Kavli, H.E. Krokan, D.W. Mosbaugh, J.A. Tainer, Crystal structure of human uracil-DNA glycosylase in complex with a protein inhibitor: Protein mimicry of DNA, Cell 82 (1995) 701–708, https://doi.org/10.1016/0092-8674(95)90467-0.

[17] A.L. Ross, J.E. Sale, The catalytic activity of REV1 is employed during immunoglobulin gene diversification in DT40, Mol. Immunol. 43 (2006) 1587–1594, https://doi.org/10.1016/j.molimm.2005.09.017.

[18] C. Rada, G.T. Williams, H. Nilsen, D.E. Barnes, T. Lindahl, M.S. Neuberger, Immunoglobulin isotype switching is inhibited and somatic hypermutation perturbed in UNG-deficient mice, Curr. Biol. 12 (2002) 1748–1755, https://doi.org/10.1016/S0960-9822(02)01215-0.

[19] E.J. Steele, Mechanism of somatic hypermutation: critical analysis of strand biased mutation signatures at A:T and G:C base pairs, Mol. Immunol. 46 (2009) 305–320, https://doi.org/10.1016/j.molimm.2008.10.021.

[20] B. Demple, T. Herman, D.S. Chen, Cloning and expression of APE, the cDNA encoding the major human apurinic endonuclease: definition of a family of DNA repair enzymes, Proc. Natl. Acad. Sci. USA 88 (1991) 11450–11454, https://doi.org/10.1073/pnas.88.24.11450.

[21] D. Lu, J. Silhan, J.T. MacDonald, E.P. Carpenter, K. Jensen, C.M. Tang, G.S. Baldwin, P.S. Freemont, Structural basis for the recognition and cleavage of abasic DNA in Neisseria meningitidis, Proc. Natl. Acad. Sci. 109 (2012) 16852–16857, https://doi.org/10.1073/pnas.1206563109.

[22] M. Bhagwat, J. a Gerlt, 3′- and 5′-Strand cleavage reactions catalyzed by the Fpg protein from Escherichia coli occur via successive beta- and delta-elimination mechanisms, respectively, Biochemistry 35 (1996) 659–665, https://doi.org/10.1021/bi9522662.

[23] H.M. Nash, S.D. Bruner, O.D. Schärer, T. Kawate, T. a Addona, E. Spooner, W.S. Lane, G.L. Verdine, Cloning of a yeast 8-oxoguanine DNA glycosylase reveals the existence of a base-excision DNA-repair protein superfamily, Curr. Biol. 6 (1996) 968–980. ⟨http://www.ncbi.nlm.nih.gov/pubmed/8805338⟩.

[24] B. Demple, L. Harrison, Repair of oxidative damage to DNA: enzymology and biology, Annu. Rev. Biochem. 63 (1994) 915–948, https://doi.org/10.1146/annurev.bi.63.070194.004411.

[25] V. Bailly, W.G. Verly, AP endonucleases and AP lyases, Nucleic Acids Res. 17 (1989) 3617–3618. ⟨http://www.ncbi.nlm.nih.gov/pmc/articles/PMC317828/⟩.

[26] C.C. RICHARDSON, I.R. LEHMAN, A. KORNBERG, A deoxyribonucleic acid phosphatase-exonuclease from Escherichia coli, J. Biol. Chem. 239 (1964) 251–258.

[27] D.S. Chen, T. Herman, B. Demple, Two distinct human DNA diesterases that hydrolyze 3′-blocking deoxyribose fragments from oxidized DNA, Nucleic Acids Res. 19 (1991) 5907–5914, https://doi.org/10.1093/nar/19.21.5907.

[28] L. Wiederhold, J.B. Leppard, P. Kedar, F. Karimi-Busheri, A. Rasouli-Nia, M. Weinfeld, A.E. Tomkinson, T. Izumi, R. Prasad, S.H. Wilson, S. Mitra, T.K. Hazra, AP endonuclease-independent DNA base excision repair in human cells, Mol. Cell. 15 (2004) 209–220, https://doi.org/10.1016/j.molcel.2004.06.003.

[29] J. Silhan, Q. Zhao, E. Boura, H. Thomson, A. Förster, C.M. Tang, P.S. Freemont, G.S. Baldwin, Structural basis for recognition and repair of the 3′-phosphate by NExo, a base excision DNA repair nuclease from Neisseria meningitidis, Nucleic Acids Res. 46 (2018) 11980–11989, https://doi.org/10.1093/nar/gky934.

[30] D.E. Barnes, T. Lindahl, Repair and genetic consequences of endogenous DNA base damage in mammalian cells, Annu. Rev. Genet. 38 (2004) 445–476, https://doi.org/10.1146/annurev.genet.38.072902.092448.

[31] A. Álvarez-Quilón, J.L. Wojtaszek, M. Mathieu, T. Patel, C.D. Appel, N. Hustedt, S.E. Rossi, B.D. Wallace, D. Setiaputra, S. Adam, Y. Ohashi, H. Melo, T. Cho, C. Gervais, I.M. Muñoz, E. Grazzini, J.T.F. Young, J. Rouse, M. Zinda, R.S. Williams, D. Durocher, Endogenous DNA 3′ blocks are vulnerabilities for BRCA1 and BRCA2 deficiency and are reversed by the APE2 nuclease, Mol. Cell. (2020) 1–14, https://doi.org/10.1016/j.molcel.2020.05.021.

[32] R. Gilboa, D.O. Zharkov, G. Golan, A.S. Fernandes, S.E. Gerchman, E. Matz, J.H. Kycia, A.P. Grollman, G. Shoham, Structure of formamidopyrimidine-DNA glycosylase covalently complexed to DNA, J. Biol. Chem. 277 (2002) 19811–19816, https://doi.org/10.1074/jbc.M202058200.

[33] K.-S. Ryu, C. Kim, I. Kim, S. Yoo, B.-S. Choi, C. Park, NMR application probes a novel and ubiquitous family of enzymes that alter monosaccharide configuration, J. Biol. Chem. 279 (2004) 25544–25548, https://doi.org/10.1074/jbc.M402016200.

[34] C. De Los Santos, M. El-khateeb, P. Rege, K. Tian, F. Johnson, Impact of the C1′ configuration of abasic sites on DNA duplex structure, Biochemistry 43 (2004) 15349–15357, https://doi.org/10.1021/bi048400c.

[35] J.A. Wilde, P.H. Bolton, A. Mazumder, M. Manoharan, J.A. Gerlt, Characterization of the equilibrating forms of the aldehydic abasic site in duplex DNA by 17O NMR, J. Am. Chem. Soc. 111 (1989) 1894–1896, https://doi.org/10.1021/ja00187a062.

[36] S. Dimitrov, Y. Koleva, T.W. Schultz, J.D. Walker, O. Mekenyan, Interspecies quantitative structure-activity relationship model for aldehydes: aquatic toxicity, Environ. Toxicol. Chem. 23 (2004) 463–470, https://doi.org/10.1897/02-579.

[37] I.G. Minko, I.D. Kozekov, T.M. Harris, C.J. Rizzo, R.S. Lloyd, M.P. Stone, Chemistry and biology of DNA containing 1,N2-deoxyguanosine adducts of the α,β-unsaturated aldehydes acrolein, crotonaldehyde, and 4-hydroxynonenal, Chem. Res. Toxicol. 22 (2009) 759–778, https://doi.org/10.1021/tx9000489.

[38] H.-S. Yu, T. Oyama, T. Isse, K. Kitagawa, T.-T.-P. Pham, M. Tanaka, T. Kawamoto, Formation of acetaldehyde-derived DNA adducts due to alcohol exposure, Chem. Biol. Interact. 188 (2010) 367–375, https://doi.org/10.1016/j.cbi.2010.08.005.

[39] E. Freese, M. Cashel, Crosslinking of deoxyribonucleic acid by exposure to low pH, BBA Spec. Sect. Nucleic Acids Relat. Subj. 91 (1964) 67–77, https://doi.org/10.1016/0926-6550(64)90171-9.

[40] J. Burnotte, W.G. Verly, Crosslinking of methylated DNA by moderate heating at neutral pH, Biochim. Biophys. Acta Nucleic Acids Protein Synth. 262 (1972) 449–452, https://doi.org/10.1016/0005-2787(72)90488-1.

[41] C. Goffin, W.G. Verly, Interstrand DNA crosslinks due to AP (apurinic/apyrimidinic) sites, FEBS Lett. 161 (1983) 140–144, https://doi.org/10.1016/0014-5793(83)80747-9.

[42] C. Goffin, S. Bricteux-Grégoire, W.G. Verly, Some properties of the interstrand crosslinks in depurinated DNA, Biochim. Biophys. Acta Gene Struct. Expr. 783 (1984) 1–5, https://doi.org/10.1016/0167-4781(84)90071-X.

[43] A.S. Prakash, N.W. Gibson, Sequence-selective depurination, DNA interstrand cross-linking and DNA strand break formation associated with alkylated DNA, Carcinogenesis 13 (1992) 425–431, https://doi.org/10.1093/carcin/13.3.425.

[44] S. Dutta, G. Chowdhury, K.S. Gates, Interstrand cross-links generated by abasic sites in duplex DNA, J. Am. Chem. Soc. 129 (2007) 1852–1853, https://doi.org/10.1021/ja067294u.

[45] A.H. Kellum, D.Y. Qiu, M.W. Voehler, W. Martin, K.S. Gates, M.P. Stone, Structure of a stable interstrand DNA cross-link involving a β- N-Glycosyl Linkage between an N6-dA amino group and an abasic site, Biochemistry 60 (2021) 41–52, https://doi.org/10.1021/acs.biochem.0c00596.

[46] N.E. Price, K.M. Johnson, J. Wang, M.I. Fekry, Y. Wang, K.S. Gates, Interstrand DNA-DNA cross-link formation between adenine residues and abasic sites in duplex dna, J. Am. Chem. Soc. 136 (2014) 3483–3490, https://doi.org/10.1021/ja410969x.

[47] N.E. Price, M.J. Catalano, S. Liu, Y. Wang, K.S. Gates, Chemical and structural characterization of interstrand cross-links formed between abasic sites and adenine residues in duplex DNA, Nucleic Acids Res. 43 (2015) 3434–3441, https://doi.org/10.1093/nar/gkv174.

[48] M. Imani Nejad, K. Housh, A.A. Rodriguez, T. Haldar, S. Kathe, S.S. Wallace, B. F. Eichman, K.S. Gates, Unhooking of an interstrand cross-link at DNA fork structures by the DNA glycosylase NEIL3, DNA Repair 86 (2020), 102752, https://doi.org/10.1016/j.dnarep.2019.102752 ((Amst)).

[49] B. Cihlova, A. Huskova, J. Böserle, R. Nencka, E. Boura, J. Silhan, High-throughput fluorescent assay for inhibitor screening of proteases from rna viruses, Molecules 26 (2021), https://doi.org/10.3390/molecules26133792.

[50] A.M. Maxam, W. Gilbert, A new method for sequencing DNA, Proc. Natl. Acad. Sci. 74 (1977) 560–564, https://doi.org/10.1073/pnas.74.2.560.

[51] T. Lindahl, An N-Glycosidase from Escherichia coli That Releases Free Uracil from DNA Containing Deaminated Cytosine Residues, Proc. Natl. Acad. Sci. 71 (1974) 3649–3653, https://doi.org/10.1073/pnas.71.9.3649.

[52] S.R.W. Bellamy, G.S. Baldwin, A kinetic analysis of substrate recognition by uracil-DNA glycosylase from herpes simplex virus type 1, Nucleic Acids Res. 29 (2001) 3857–3863.

[53] S.J. Admiraal, P.J. O'Brien, Base excision repair enzymes protect abasic sites in duplex DNA from interstrand cross-links, Biochemistry 54 (2015) 1849–1857, https://doi.org/10.1021/bi501491z.

[54] M.J. Catalano, S. Liu, N. Andersen, Z. Yang, K.M. Johnson, N.E. Price, Y. Wang, K. S. Gates, Chemical structure and properties of interstrand cross-links formed by reaction of guanine residues with abasic sites in duplex DNA, J. Am. Chem. Soc. 137 (2015) 3933–3945, https://doi.org/10.1021/jacs.5b00669.

[55] J.G. Varela, L.E. Pierce, X. Guo, N.E. Price, K.M. Johnson, Z. Yang, Y. Wang, K. S. Gates, Interstrand cross-link formation involving reaction of a mispaired cytosine residue with an abasic site in duplex DNA, Chem. Res. Toxicol. 34 (2021) 1124–1132, https://doi.org/10.1021/acs.chemrestox.1c00004.

[56] P.D. Chastain, J. Nakamura, S. Rao, H. Chu, J.G. Ibrahim, J.A. Swenberg, D. G. Kaufman, Abasic sites preferentially form at regions undergoing DNA replication, FASEB J 24 (2010) 3674–3680, https://doi.org/10.1096/fj.09-145276.

[57] K.N. Mohni, S.R. Wessel, R. Zhao, A.C. Wojciechowski, J.W. Luzwick, H. Layden, B. F. Eichman, P.S. Thompson, K.P.M. Mehta, D. Cortez, HMCES maintains genome integrity by shielding abasic sites in single-strand DNA, Cell 176 (2019) 144–153, https://doi.org/10.1016/j.cell.2018.10.055, e13.

[58] S. Boiteux, F. Coste, B. Castaing, Repair of 8-oxo-7,8-dihydroguanine in prokaryotic and eukaryotic cells: properties and biological roles of the Fpg and OGG1 DNA N-glycosylases, Free Radic. Biol. Med. 107 (2017) 179–201, https://doi.org/10.1016/j.freeradbiomed.2016.11.042.

[59] N. Wang, H. Bao, L. Chen, Y. Liu, Y. Li, B. Wu, H. Huang, Molecular basis of abasic site sensing in single-stranded DNA by the SRAP domain of E. coli yedK, Nucleic Acids Res. 47 (2019) 10388–10399, https://doi.org/10.1093/nar/gkz744.

[60] K.P. Roberts, J.A. Sobrino, J. Payton, L.B. Mason, R.J. Turesky, Determination of Apurinic/Apyrimidinic Lesions in DNA with High-Performance Liquid Chromatography and Tandem Mass Spectrometry, Chem. Res. Toxicol. 19 (2006) 300–309, https://doi.org/10.1021/tx0502589.

[61] J. Guo, H. Chen, P. Upadhyaya, Y. Zhao, R.J. Turesky, S.S. Hecht, Mass SPectrometric Quantitation of Apurinic/Apyrimidinic Sites in Tissue DNA of Rats Exposed to Tobacco-Specific Nitrosamines and in Lung and Leukocyte DNA of Cigarette Smokers and Nonsmokers, Chem. Res. Toxicol. 33 (2020) 2475–2486, https://doi.org/10.1021/acs.chemrestox.0c00265.

[62] H. Chen, L. Yao, C. Brown, C.J. Rizzo, R.J. Turesky, Quantitation of apurinic/apyrimidinic sites in isolated DNA and in Mammalian tissue with a reduced level of artifacts, Anal. Chem. 91 (2019) 7403–7410, https://doi.org/10.1021/acs.analchem.9b01351.

[63] S. Bennett, J. Kitner, Characterization of the aldehyde reactive probe reaction with AP-sites in DNA: Influence of AP-lyase on adduct stability, Nucleosides Nucleotides Nucleic Acids 25 (2006) 823–842, https://doi.org/10.1080/15257770600726133.

[64] K. Nagorska, J. Silhan, Y. Li, V. Pelicic, P.S. Freemont, G.S. Baldwin, C.M. Tang, A network of enzymes involved in repair of oxidative DNA damage in Neisseria meningitidis, Mol. Microbiol. 83 (2012) 1064–1079, https://doi.org/10.1111/j.1365-2958.2012.07989.x.

[65] B. Landova, J. Silhan, Conformational changes of DNA repair glycosylase MutM triggered by DNA binding, FEBS Lett. 594 (2020) 3032–3044, https://doi.org/10.1002/1873-3468.13876.

[66] L.T. Da, J. Yu, Base-flipping dynamics from an intrahelical to an extrahelical state exerted by thymine DNA glycosylase during DNA repair process, Nucleic Acids Res. 46 (2018) 5410–5425, https://doi.org/10.1093/nar/gky386.

[67] P.S. Thompson, K.M. Amidon, K.N. Mohni, D. Cortez, B.F. Eichman, Protection of abasic sites during DNA replication by a stable thiazolidine protein-DNA cross-link, Nat. Struct. Mol. Biol. 26 (2019) 613–618, https://doi.org/10.1038/s41594-019-0255-5.

81

Model of abasic site DNA cross-link repair; from the architecture of NEIL3 DNA binding domains to the X-structure model

Andrea Huskova[1], Dhurvas Chandrasekaran Dinesh [1], Pavel Srb[1], Evzen Boura [1], Vaclav Veverka[1,2] and Jan Silhan [1,*]

[1]Institute of Organic Chemistry and Biochemistry of the Czech Academy of Sciences, Flemingovo namesti 2, 166 10 Prague, Czech Republic and [2]Department of Cell Biology, Faculty of Science, Charles University, Prague, Czech Republic

ABSTRACT

Covalent DNA interstrand crosslinks are toxic DNA damage lesions that block the replication machinery that can cause a genomic instability. Ubiquitous abasic DNA sites are particularly susceptible to spontaneous cross-linking with a base from the opposite DNA strand. Detection of a crosslink induces the DNA helicase ubiquitination that recruits NEIL3, a DNA glycosylase responsible for the lesion removal. NEIL3 utilizes several zinc finger domains indispensable for its catalytic NEI domain repairing activity. They recruit NEIL3 to the repair site and bind the single-stranded DNA. However, the molecular mechanism underlying their roles in the repair process is unknown. Here, we report the structure of the tandem zinc-finger GRF domain of NEIL3 and reveal the molecular details of its interaction with DNA. Our biochemical data indicate the preferential binding of the GRF domain to the replication fork. In addition, we obtained a structure for the catalytic NEI domain in complex with the DNA reaction intermediate that allowed us to construct and validate a model for the interplay between the NEI and GRF domains in the recognition of an interstrand cross-link. Our results suggest a mechanism for recognition of the DNA replication X-structure by NEIL3, a key step in the interstrand cross-link repair.

INTRODUCTION

DNA interstrand cross-links (ICLs) are toxic DNA lesions that can arise from various endogenous and exogenous sources (e.g. *cis*-platinum, mitomycin C, acetaldehyde and formaldehyde) and ICLs can also form spontaneously from an abasic site (1–3). Inevitably, such a diverse chemical na-ture of cross-linking agents is reflected by a multitude of different structures of individual ICLs (4–8).

Abasic site interstrand cross-links (Ap-ICLs) arise spontaneously from naturally occurring abasic (Ap) sites. An aldehyde group of the ring-opened ribose at C1′ forms an *N*-glycosidic bond with an amine group of a base in the opposite DNA strand (9,10). It is noteworthy that a stable and specific Ap-ICL forms between an Ap site and an adenine in the opposite strand within the 5′-Ap-dT-3′ sequence (11,12).

ICLs pose impenetrable barriers to DNA replication, and the ICLs must be removed by specialized DNA repair pathways to prevent their deleterious effects. Initially, the Fanconi anaemia (FA) DNA repair pathway was identified in the repair of the ICL (13–15). Mutations in one of the many FA genes lead to Fanconi anaemia, a rare genetic disease characterized by chromosomal abnormalities, bone marrow failure and a strong predisposition to cancer. The cellular and molecular hallmark of FA is a sensitivity to cross-linking agents which leads to its implication with the ICL repair (16–18). Later, with the emergence of the Ap-ICL, an alternative, non-canonical or NEIL3 (Nei endonuclease VIII-like 3) pathway was discovered (19). FA pathway described in J.C. Walter's laboratory was a prerequisite for the discovery of the NEIL3 pathway of ICL repair (19).

NEIL3 has a catalytic NEI domain and belongs to the Fpg/Nei DNA glycosylase family. The enzymes from this family are structural and functional homologues, and they are conserved from bacteria to humans (20,21). Their generic role in base excision repair (BER) is to remove single base lesions arriving mainly from oxidative stress (22). In mammals, three NEIL (Nei endonucleases VIII-like) DNA glycosylases were identified: NEIL1, NEIL2 and NEIL3 (23–26). In general, Nei enzymes are bi-functional glycosylases, with glycosylase and Ap-lyase activities. The first step of catalysis is a nucleophilic attack on an *N*-glycosidic bond of the damaged base and its release. The enzyme then

forms a covalent link (Schiff-base) with the orphaned ribose of the damaged DNA strand. In the second and slower step, phosphodiester bonds of the DNA are broken due to a β or β-δ elimination mechanism (Ap-lyase activity), generating a toxic 3′-DNA lesion and a single-strand DNA break (27–30).

Initially, NEIL3 was reported to have poor Ap-lyase activity on substrates with double-stranded DNA (dsDNA). Surprisingly, higher activity and therefore specificity was observed for single-stranded DNA (ssDNA) substrates (20). It has been shown that NEIL3 binds to the telomere sequence via its C-terminus and protects telomere integrity in proliferating cells within the S/G2 phase (31). Interestingly, NEIL3 was found to participate in the repair of the Ap-ICL. In *Xenopus* egg extracts, the Ap-ICL was unhooked when one of the two *N*-glycosidic bonds forming the ICL was cleaved by NEIL3. *N*-glycosyl cleavage by NEIL3 is the primary unhooking pathway for the Ap-ICL (19).

NEIL3 is the only member of the Fpg/Nei glycosylase family with an elongated C-terminus and it contains three sets of zinc finger domains (NEI, NZF and GRF domains 1 and 2) (Figure 1A). The N-terminal NEI domain is responsible for the DNA glycosylase repair activity on the Ap-ICL (19). The NLP4-type zinc finger (NZF) is a ubiquitin-binding domain employed in the recruitment of NEIL3 glycosylase to an Ap-ICL via TRAIP-dependent ubiquitylation of CMG helicase. NZF is required for efficient Ap-ICL repair in *Xenopus* extracts *ex vivo*. However, the NZF domain is not essential for enzymatic unhooking of DNA cross-links on model substrates *in vitro* (32).

The other two zinc finger domains (GRF1 and GRF2) are homologues with the 'GRF' zincfinger from APEX2 Ap endonuclease. GRFs are known to interact with ss-DNA (33). The GRF name originates from the triad of conserved residues: Gly (G), Arg (R) and Phe (F). However, in GRF2, the Arg is replaced with Lys, which is distinct from the APEX2 GRF motif (Figure 1B). Interestingly, lysine (K553) in GRF2 disrupted the binding with short ssDNA (34). The crystal structure of the human GRF1-GRF2 dimer revealed a shape resembling a butterfly. These two GRF domains together were able to bind ssDNA with greater affinity than individual domains via their avidity (35). Experiments in *Xenopus* extracts have shown that GRF domains play a role in efficient Ap-ICL unhooking, and they are required for the efficient recruitment of NEIL3 to the stalled replication fork on the Ap-ICL. In the absence of GRFs, the unhooking reaction was compromised. This indicated that the GRFs' role in Ap-ICL repair might be the proper recognition of the crosslinked substrate (32). In contrast, another study has revealed that GRF domains inhibit the enzymatic activity of NEIL3 *in vitro* (35). These seemingly contradictory observations suggest that the mechanistic role of the GRF domain in Ap-ICL repair is more complex, and it is yet to be explained.

In this study, we investigated the molecular architecture of recognition of the stalled replication fork by NEIL3 DNA glycosylase during Ap-ICL repair. We obtained two structures of GRF domains with and without ssDNA from restraints from NMR measurements. We observed that the GRF domains recognize not only ssDNA as reported previously but also very short replication-fork intermediates.

The GRF1&2 domains bind to the 5′-ssDNA overhangs of the DNA duplex with a slight preference. These observations indicate that GRFs may play a role in the recognition of native Ap-ICL DNA substrates.

To understand the architecture of Ap-ICL repair, we crystallized and solved the structure of the NEI domain from mouse NEIL3, covalently trapped with the DNA substrate. We observed that, unlike GRF domains, the NEI domain recognises 3′-ssDNA overhangs on duplex or fork DNA structures. Based on our structural, biochemical and enzymological data, and with the use of AlphaFold, we constructed a model of NEIL3 bound to the replication fork in the intermediate state. This data shed light on the repair scenario of Ap-ICL repair on the stalled replication fork. In this model, we considered two collided DNA replication forks that arise from bidirectional replication, forming a letter X (14,19). Our data suggest a possible mechanism by which NEIL3 recognizes the DNA replication X-structure. The data also indicate the role of GRF and NEI domains in the recognition of the native Ap-ICL substrate.

MATERIALS AND METHODS

Cloning, expression and purification of the recombinant GRF and NEI protein domains

The GRF and NEI domains were amplified from the full-length mouse NEIL3 gene NM_146208 (Origene). PCR products were cloned using Gibson assembly (36). The tandem GRF1&GRF2 domains (505–597) were cloned into a pSUMO vector with an N-terminal His_{8x}-SMT3 tag. The NEI domain (1–282) was cloned into a modified pET-24b vector with a C-terminal 3C protease (HRV) site and subsequent His_{6x} tag. The proteins were expressed and purified using standard protocols (37,38). Briefly, the plasmids were transformed into *Escherichia coli* BL21 Star™ (DE3) cells (ThermoFisher). Small 5 ml cultures were grown overnight at 37°C in LB medium. Expressions were carried out after inoculation of ZY5052 autoinduction media supplemented with 50 μM $ZnSO_4$. After reaching an optical density of $OD_{600} = 0.6–1$ at 37°C, the temperature was lowered to 18°C, and the culture was grown overnight. The harvested cells were lysed by sonication in a lysis buffer containing 20 mM Tris–HCl pH 8.0; 300 mM NaCl, 30 mM imidazole pH 8.0, 10% glycerol and 1 mM tris(2-carboxyethyl)phosphine (TCEP). The supernatant was separated by centrifugation, incubated with 2 ml of Ni-NTA resin (Machery-Nagel), and extensively washed with the lysis buffer using the batch technique. The proteins were eluted with the lysis buffer supplemented with 300 mM imidazole pH 8.0.

The proteins were desalted on a HiPrep 26/10 desalting column (GE Healthcare) and loaded on a cation exchange HiTrap SP HP column equilibrated with buffer A (20 mM Tris–HCl pH 8.0, 125 mM NaCl, 10% glycerol, 2 mM β-mercaptoethanol (β-ME)). In the case of the NEI protein, 70 mM NaCl was used for buffer A. The proteins were eluted by gradients of NaCl. The solubility tag GRF domain was cleaved by SUMO protease from yeast (Ulp1), and after overnight incubation at 4°C, the sample was desalted and reloaded on cation exchange as described above. The proteins were purified on size-exclusion Superdex 75 In-
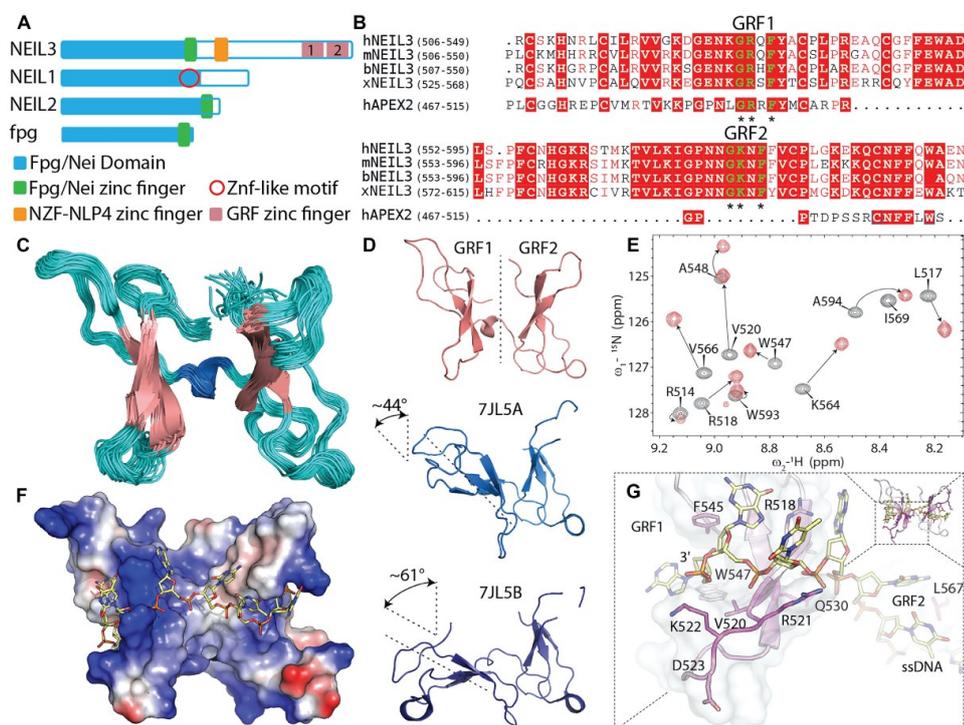
Figure 1. NMR-based structure of GRF domains in complex with ssDNA. (**A**) Schematics of the domain organisation of NEIL3, NEIL2, NEIL1, NEI/Fpg domain (blue), two GRF domains GRF1 and GRF2 (pink blocks) NEIL3 are located at the C-terminus, schematics bacterial fpg added for comparison. (**B**) Sequence alignment of GRF 1&2 from different organisms in comparison with single GRF domain from hAPEX2. Asterisks denote the GRF motif. (**C**) NMR ensemble of mouse GRF 1&2 pseudo dimer (loops in pink, b-sheets in magenta, and linking a-helix in cyan) (PDB ID 7OMK, Supplementary Table S1). (**D**) A comparison of inter-domain rearrangements of mouse NEIL3 GRF 1&2 (pink) and human NEIL3 GRF1&2 domains, two dimer molecules were present in the asymmetric unit of crystal structure PDB ID-7JL5 (light and dark blue) (35), human GRF1 was aligned to mouse GRF1, the angle difference for GRF2 (chain A) was 43.9° with lateral displacement of 9.5Å and GRF2 (chain B) was 61.4° with a displacement of 11.2 Å. (**E**) Selected ^{1}H–^{15}N HSQC spectral overlay of free mGRF (black cross-peaks) and GRF:ssDNA complex (red cross-peaks). (**F**) Electrostatic surface potential of GRF:ssDNA complex (ssDNA yellow sticks). (**G**) Detail of the residues responsible for GRF:DNA interaction (R518, V520, (R521) and W547 from panel (E) and highest chemical shift perturbations shown as the gradient of magenta (more detail is shown in Supplementary Figure S3).

crease GL HiLoad 10/300 (GE Healthcare) in buffer A. The purity of the proteins was verified on SDS-PAGE in a 15% polyacrylamide gel, stained with Coomassie brilliant blue. The proteins were concentrated and flash-frozen in $N_2(l)$ and kept at –80°C.

Isotopically labelled GRF protein for NMR experiments was expressed using the minimal medium containing [^{15}N] NH_4Cl, and [^{13}C] glucose supplemented with 0.1 μg/ml of ampicillin, 20 μM $ZnSO_4$, 1 mM $MgCl_2$ and 10 μM $FeCl_2$ in citric acid. Inoculated cells were incubated in a shaker at 37°C. After reaching an OD_{600} of 0.6, protein expression was induced with 600 μM isopropyl β-D-1-thiogalactopyranoside (IPTG), the temperature was lowered to 18°C and the culture was grown overnight. Labelled protein was purified as mentioned previously.

NMR spectroscopy

NMR spectra were acquired at 25°C using an 850 MHz Bruker Avance spectrometer, equipped with a triple-resonance (^{15}N/^{13}C/^{1}H) cryoprobe. The sample volumes were either 0.16 or 0.35 ml, in 12.5 mM NaPhos pH 6.5, 50 mM NaCl, 1 mM TCEP, 5% D_2O/90–95% H_2O. A series of double- and triple-resonance spectra (39,40) were recorded to obtain sequence-specific resonance assignment. in NMRFAM-SPARKY (Lee *et al.*, 2015). ^{1}H–^{1}H distance restraints were derived from the 3D ^{15}N/^{1}H NOESY-HSQC and ^{13}C/^{1}H NOESY-HMQC spectra using a NOE mixing time of 100 ms.

The structural calculation was carried out in CYANA (41) using NOESY data in combination with backbone torsion angle restraints, generated from assigned chemi-

cal shifts using the program TALOS+ (42). The combined automated NOE assignment and structure determination protocol (CANDID) was used for automatic NOE cross-peak assignment. Subsequently, five cycles of simulated annealing combined with redundant dihedral angle restraints were used to calculate a set of converged structures with no significant restraint violations (distance and van der Waals violations < 0.5Å and dihedral angle constraint violations < 5°). The 35 structures with the least restraint violations were further refined in explicit solvent using YASARA (43) and subjected to further analysis using the Protein Structure Validation Software suite (www.nesg.org). The statistics for the resulting structure are summarized in Supplementary Table S1-1. The structures, NMR restraints and resonance assignments were deposited in the Protein Data Bank (PDB ID 7OMK) and BMRB (accession code: 34630). The relaxation data were obtained using the 300 μM ^{15}N labeled sample. The relaxation delays were 0.0448, 0.0672, 0.112, 0.179, 0.246, 0.381, 0.784, 1.23 s for R1 and 0, 0.0310, 0.0628, 0.0931, 0.124, 0.186, 0.279 s for R2 measurements. The recovery delay was set to 1.2 s with 4 or 8 scans per FID. The {^{1}H}–^{15}N steady state nuclear Overhauser enhancement (NOE) was measured in an interleaved manner using a 5 s long train of selective 180° pulses for proton irradiation, separated by 22 ms delays (44), and centered at 8.2 ppm in order to avoid water saturation. The offset of these pulses was shifted by 50 kHz in the reference experiment to ensure constant sample heating (44,45).

To follow changes in the protein spectra upon DNA binding, we calculated chemical shift perturbations (CSPs). The CSP of each assigned resonance in the 2D ^{15}N/^{1}H HSQC spectra of the protein in the free state was calculated as the geometrical distance in ppm to the peak in the 2D ^{15}N/^{1}H HSQC spectra acquired under different conditions using the formula (1);

$$\delta\Delta = \sqrt{\Delta^2_H \delta + (\Delta.\alpha)^2} \quad (1)$$

where α is a weighing factor of 0.2 used to account for differences in the proton and nitrogen spectral widths (46).

Gel-based and fluorescent anisotropy DNA binding assays

A specific three-letter code (NTX code) was used to name the oligonucleotides used in the binding assays. The NTX code indicates that N stands for the number of ssDNA nucleotides of the single-stranded arm of the DNA structure, T for thymidine, and X for the shape of ssDNA structure (Y fork, 3′ or 5′ overhangs).

Labelled (FAM) and unlabelled DNA oligonucleotides were custom synthesized (Microsynth, Switzerland), and the DNA sequences are listed in Supplemental Figure 1. Fluorescent dye FAM-dT was placed instead of adenine (x) in the apex of the hairpin 5′-GACGCGxAGCGTC-3′. DNA oligos were resuspended in TES buffer: 10 mM Tris–HCl pH 8.0, 50 mM NaCl, 1 mM EDTA. Double-stranded DNA substrates were prepared by mixing equimolar amounts of complementary strands, which were heated to 95°C and allowed to anneal by slow cooling to room temperature. The hairpin substrates were heated to 95°C and then rapidly cooled on ice.

Native EMSA was performed as follows; 5 μM labelled or unlabelled DNA and 5 μM GRF were mixed and incubated for 30 min at 25°C in 20 mM NaH$_2$PO$_4$ pH 6.5, 100 mM NaCl, 10% glycerol and 1 mM TCEP. Samples were then separated by electrophoresis on 15% native polyacrylamide gels (1× TBE, 15% polyacrylamide/bisacrylamide 14:1). The gels with unlabelled DNA were stained with Coomassie Brilliant Blue to visualize the GRF:DNA complex and were analyzed using the commercial software ImageQuant TL. Gel lines of constant width were manually selected and background subtraction was performed using the rolling sphere method. Bands with constant dimensions containing the binding product were selected manually. The values for each gel band were plotted on a graph. All gels were scanned at Typhoon LASER imager (GE).

Fluorescence anisotropy binding assays were performed as a titration series with a constant concentration of FAM-labelled DNA (50 nM) mixed with pure GRF1&2 protein at a final concentration of 0 nM to 20 000 nM. Fluorescent anisotropy binding measurements were performed on a TECAN Infinite M1000 Microplate Reader (Tecan Group Ltd.) at 25°C in 20 mM NaH$_2$PO$_4$ pH 6.5, 100 mM NaCl, 10% glycerol and 1 mM TCEP. The excitation wavelength was $\lambda = 470$ nm and the emission $\lambda = 520$ nm. The total intensity was calculated according to the following formula (2)

$$Itot = Ivv + 2*G*Ivh \quad (2)$$

where G is the G-factor, which depends on the optical system of the instrument, was measured to be 1.194. G-factor was measured according to a protocol on the TECAN with input polarisation value (mP) of free DNA, which was measured on the Fluoromax-4 spectrofluorimeter (Horiba, Scientific). The fraction of DNA bind (f_B) was determined according to formula (3)

$$fB = \frac{(Aobs - Amin)}{(Amax - Aobs)*Q + (Aobs - Amin)} \quad (3)$$

where $Aobs$ is the observed anisotropy for a given concentration of GRF, $Amin$ is the minimum observed anisotropy and $Amax$ is the anisotropy at saturation (47,48). The correlation of quantum yield (Q) represents the ratio of total intensities (Itot) of bound to free fluorophore. Dissociation constants were calculated as described previously (49), using formula (4)

$$fB = ([DNA]/2)(KD + [DNA] + [GRF])$$
$$- \sqrt{\left(KD + [DNA] + [GRF]^2\right) - 4[DNA][GRF]} \quad (4)$$

where K_D is an apparent dissociation constant and the values in parentheses, e.g. [DNA], are the concentrations at a given point in the titration. This model for the fit is an approximation as in case of many DNA binding proteins unspecific binding is observed during the titration. Non-linear

fitting of the data was performed using Graphpad Prism (GraphPad Software).

DNA and NEIL3 trapping assay

DNA oligonucleotides (sequences are shown in Supplementary Figure S1) were annealed as previously mentioned. For abasic site creation, 0.5 U uracil–DNA glycosylase (UDG) (New England Biolabs) was added per one sequence reaction and kept for 20 min at room temperature. 250 nM DNA substrates and 200 nM NEIL3 were incubated in the presence of 100 mM $NaBH_3CN$ in 20 mM HEPES 7.0, 50 mM NaCl and 1 mM TCEP at 25°C. At given time points, 30 µl of the reaction was taken and mixed with 5× SDS of sample buffer (60 mM Tris pH 6.8, 25% (v/v) glycerol, 2.9% (w/w) SDS, 0.1% (v/v) Bromphenol Blue, 714 mM β-ME) to terminate the reaction. These samples were resolved on a 15% SDS-PAGE.

Crystallization and structure determination

DNA hairpin substrates for crystallographic experiments were synthesized with the following sequences: 5′ overhang 5′-TTTTTTUACGCGAAGCGTG-3′ and 3′ overhang. The DNA (250 µM) hairpin substrates were annealed by being heated to 95°C for 5 min and then rapidly placed on ice. 300 µl of annealed DNA was treated with 3 µl of UDG (NEB) and incubated at RT to generate the Ap site. Subsequently, 300 µl of purified NEI domain (300 µM) supplemented with 200 mM $NaBH_3CN$ was added. The reaction was allowed to proceed for 1 h to form the trapped NEI:DNA complex. The progress of the reaction was checked on 15% SDS-PAGE gels. The reaction mixture was desalted on a 5 mL HiTrap Desalting column (Cytiva) and loaded onto a 5 ml HiTrap Q HP column (Cytiva) equilibrated with 20 mM Tris–HCl pH 8.0 and 50 mM NaCl, 1 mM TCEP. The column was eluted with a linear gradient of NaCl. The trapped complex was loaded on Superdex 200 Ⓡ Increase 10/300 GL (Cytiva). The fractions containing NEI:DNA intermediate were concentrated to roughly 200 µM ($OD_{260\,nm}$ = 30).

The crystals were grown at 22°C using the sitting drop method where 200 nL trapped complex was mixed with 200 nL with a reservoir solution containing 50 mM PIPES pH 7.5, 4% (w/v) PEG 8000 20 mM $MgCl_2$ and 1 mM spermine. Crystals were soaked for approx. one minute in 20% glycerol supplemented in the reservoir. The cryoprotective condition was prepared by mixing 8 µl of the reservoir with 2 µl of glycerol. Mounted crystals were flash-frozen in liquid nitrogen. All datasets were collected at synchrotron beamline MX 14.2 at BESSY II Helmholtz–Zentrum Berlin, Germany. They were indexed with XDS directly at the beamline (50). Data were scaled with Aimless (51). The molecular replacement was carried out in Phaser software using the structure of the mNEIL3 NEI domain as a model PDB ID = 3W0F (52). The structures were refined using Refine, and the models were manually edited in Coot. All three programs were implemented in the Phenix package (53,54). Data collection and model refinement statistics are listed in Supplementary Table S2. The structure figures were generated using PyMOL (http://www.pymol.org/).

RESULTS

The structure of GRF determined by NMR spectroscopy

We have obtained the NMR structure of GRF1 and GRF2 domains of mouse NEIL3. The overall fold of previously reported crystal structures of individual human GRF domains is in good agreement with our NMR structure (35). The RMSD between mouse and human GRF domains RMSD (GRF1) = 1.94Å and whilst the RMSD (GRF2) = 0.87Å. However, some structural differences were observed mainly in the loop regions. Each domain consists of three antiparallel beta-sheets with a zinc finger region. Two GRF domains are positioned into a butterfly-like structure connected with a short helix linker (Figure 1C). It is noteworthy that interdomain organisation is different for the crystal structure of GRFs from human NEIL3 and our structure (Figure 1C). In the case of the previously published structure of human GRF, two molecules of GRF1&2 occupy the asymmetric unit, and each of the GRF pairs makes a different angle between the domains (Figure 1D) (35).

The structure of single-stranded DNA bound to NEIL3 GRF pseudo-dimer

The ability of GRF domains to bind single-stranded DNA is a well-documented feature (33,55). We set out to understand the role of GRF domains in DNA repair and we have obtained the structure of mouse GRF1&2 pseudo-dimer in the presence of DNA using NMR spectroscopy.

We attempted to obtain this structure with ssDNA oligonucleotide. We carried out NMR titrations of short oligonucleotides ssDNA. The isotopically unlabelled DNA (7mer 3′-GTCATGA-5′) was titrated with $^{13}C-^{15}N$ isotopically labelled GRF protein. Overlay of the $^{1}H-^{15}N$ HSQC spectra of a free and DNA bound revealed residues that were significantly perturbed by DNA interaction (Supplementary Figure S3). We triangulated the position of the DNA backbone bound to GRF and generated a data-driven HADDOCK model of their complex (Figure 1). The lowest energy structure ensemble of GRF pseudo-dimer displays a relatively rigid structure without any significant interdomain rearrangements. In GRF:DNA complex structure, the DNA is oriented from its 5′ end, located at GRF2, to the 3′ end leaning over the GRF1. In the middle of the DNA, there is a junction of GRF dimers, and there is little to no interaction between the two (Figure 1).

We believe that there is a reason for the butterfly arrangement of NEIL3 GRF1&2. The crystal structure of *E. coli* Topoisomerase 1 (PDB ID 4RUL) contains five GRF-like ssDNA binding domains which are organized in a series that stimulates its enzymatic activity (Supplementary Figure S2) (55). The fold of these zinc-ribbon (ZR) domains (TOP1-ZR1-ZR5) resembles the fold of the GRF domain. Three ZRs contain zinc, while the other two are zinc-less. A structural overlay of these domains with our GRF:DNA structure reveals that TOP1 ZR domains are arranged along with DNA in parallel to each other (Supplementary Figure S2). On the other hand, the butterfly pseudo-dimer of GRF has an antiparallel arrangement. Moreover, the interlink joining GRF1&2 domains seems to be unique, and no such arrangement can be seen in the solved crystal structure

of Topoisomerase 1 (*E. coli*). Neither pair of these TOP1 ZR domains has an interdomain arrangement that is similar to NEIL3 GRF1&2. The DNA binds to the GRF domains in such a way that the domains can bind to either strand or to even both strands, at the replication fork.

GRFs recognition of single-stranded DNA

First, the focus was to determine the minimal length of ss-DNA oligonucleotide recognised by the pair of the GRF domains. NMR titrations have shown that the optimal length of an ssDNA oligo was ∼7–9 nt. To assess interactions with ssDNA, we employed a semi-quantitative electrophoresis mobility shift assay (EMSA). Due to the opposite charge of GRF, the GRF:DNA complexes with short ssDNA oligonucleotides up to 11 nt long did not migrate into the PAGE gel. Therefore, we used a dsDNA hairpin (DNAhp, 13 nt long) as a substrate with ssDNA 5′ and 3′ overhangs. Using DNAhp increased the overall negative charge of the complex and improved mobility within the gel. The DNAhp oligonucleotides contained ssDNA 5′ and 3′ oligo-dT overhangs that were 0, 2, 4, 6, 8, 10 or 12 nt long (Supplementary Figures S1 and S4). The breaking point where the complex formation was observed in the gel was at around 4 nt. Next, we performed qualitative EMSA assays to assess GRF binding with DNA forks and tested the effect of fluorescent dye on the DNA binding. We did not observe significant differences in the binding of FAM-labelled versus unlabelled DNA (Supplementary Figure S4). We then performed a fluorescence anisotropy binding assay to quantitatively compare DNA and compared GRF binding to 5′ and 3′ ssDNA overhangs. Repeatedly, the binding constants for oligonucleotides with 5′ and 3′ ssDNA overhang, were comparable. We observed a slightly greater affinity of GRF domains towards oligonucleotides with 5′ ssDNA overhang. In the control experiment, there was significantly weaker binding between the dsDNA helix and GRF domain, confirming specificity for ssDNA (Figure 2A).

GRF and interaction with replication-like structures

The architecture of GRF1&2 suggests that two different DNA chains could bind each domain, such as each arm of the DNA replication fork. To test this hypothesis, we tested the interaction of DNA replication-like structures with GRF1&2. We have designed small DNA forks with short ssDNA arms of identical length with DNA duplexes with hairpin ends to ensure all oligos were annealed (Supplementary Figure S1). The length of ssDNA arms at both 5′ and 3′ ends, arms of the fork, were 0, 1, 2, 3 or 4 nucleotides long. We performed qualitative EMSA assays to assess GRF binding with DNA forks and then performed a fluorescence anisotropy binding assay to quantitatively verify binding to the DNA forks and compared it to DNA oligonucleotides with ssDNA overhangs. GRF1&2 was able to bind well to a replication fork DNA substrate with short ssDNA arms (Figure 2B). In the case of all 2TY, 3TY, and 4TY GRF1&2 bound significantly better to these forks rather than to 3T3′ or 3T5′ oligonucleotides (and to 4T3′ and 4T5′ respectively) with ssDNA overhangs of the same length (Figure 2B). Moreover, the affinity GRF1&2 was

greater for forks than for the oligos with ssDNA overhangs with an identical total number of nucleotides (e.g. 4TY versus 8T3′ or 8T5′). As GRF1&2 binds to the fork structures of a shorter length better than to the simple overhang, this suggests that both arms of the fork may be involved in the binding. Because the migration of GRF:fork-DNA on a native PAGE gel was similar to the GRF complex with an ssDNA overhang, we hypothesise that each GRF domain binds to one side of the fork.

GRF and the binding of replication fork with DNA damage

To further investigate the role of GRF in the Ap-ICL repair we tested how the presence of DNA damage (Ap site) affects the DNA-protein interaction. Similarly like in experiments in Figure 2A, DNAhp with ssDNA overhang at either end were used. Ap site as DNA damage was placed in the duplex close to the branching point as indicated in Supplementary Figures S4 nd S5. In native EMSA DNA binding experiments, we observed a preference of the GRF domains for the 5′ ssDNA overhang. However, from quantitative K_D measurement, the binding of 5′ ssDNA overhang was only slightly increased by the presence of the damage site in DNA. This was observed in both cases with the damage located either on the top or the bottom DNA strand. This experiment demonstrated a subtle selectivity for the 5′ end, and it did not suggest that the presence of DNA damage alterations in the vicinity of the fork branching accentuate these differences (Supplementary Figures S4 and S5).

Single-stranded DNA at the 3′-end of the lesion is required for the efficient catalytic activity of NEIL3

The NEI domain of NEIL3 glycosylase has been reported to have a substrate (Ap-ICL) preference when catalysing the repair. The original Ap site of the crosslink is located on the 3′-arm of the replication fork (56). To understand the role of the individual arms of the fork, we carried out enzymatic assays with a simplified DNA replication fork with only one ssDNA overhang (fork) present. We have used the Ap site within the DNA duplex substrates with 3′ or 5′ overhangs 6 nt long (6T). The Ap sites were generated by UDG treatment of uracils placed in the duplex at the branching point. The reaction of the Ap site containing substrates with the NEI domain was terminated by the excess of $NaBH_3CN$ covalently cross-linking the NEI domain to the DNA, forming a DNA–protein crosslink. The reactions were resolved on an SDS-PAGE gel. NEI enzymatic assays revealed a 33-fold rate enhancement using the substrate with the 3′ overhang versus the 5′ overhang (Figure 3) (56). These experiments demonstrate that ssDNA is required in the 3′ direction of the Ap site for efficient catalysis.

Crystal structure of abasic site DNA intermediate with mNEIL3 NEI domain

To solve the structure of the complex of mNEIL3 with a DNA substrate, we expressed and purified the N-terminal domain of mNEIL3 1–282 (NEI domain). We prepared and set up crystallization plates with covalently trapped complexes of NEI-DNA. The stable trapped complex was prepared by reducing the Shiff-base intermediate of the repair
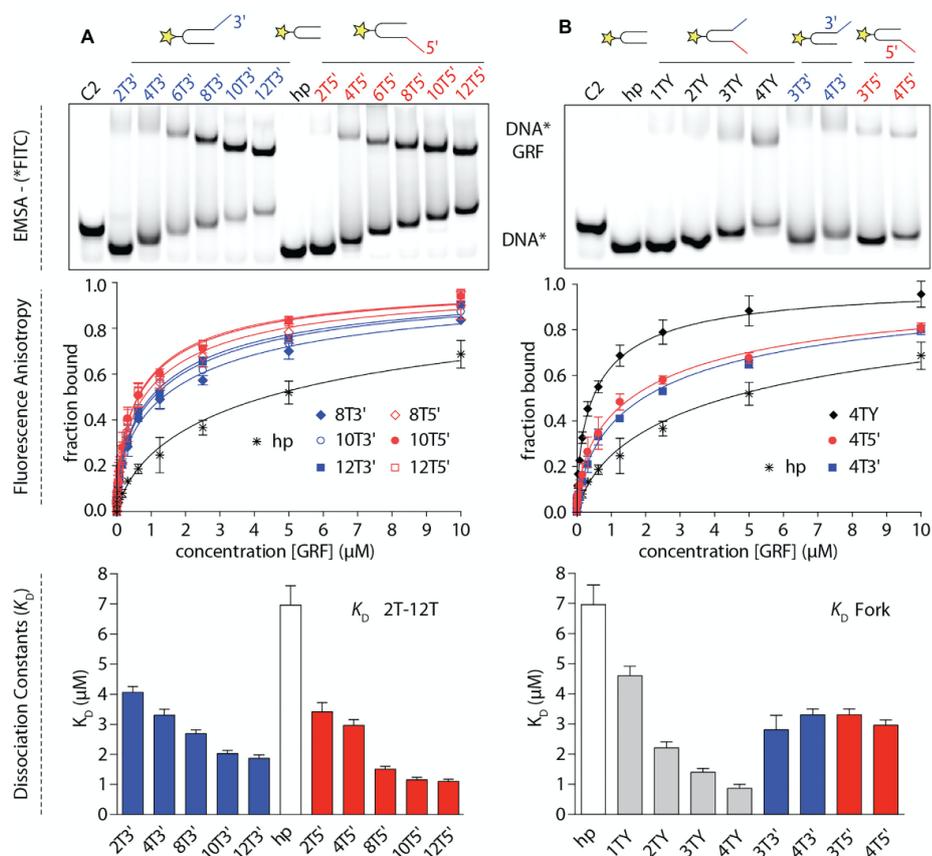
Figure 2. GRF domain, DNA binding from single-stranded DNA to recognition of DNA fork. Binding of GRF1&2 to FAM-labelled (star) DNA duplexes with 3′ (blue) and 5′ (red) ssDNA overhangs. (**A**) Comparative binding of GRF to DNA with different lengths of 3′ and 5′ overhangs. The K_D value decreases with increasing 3′ and 5′ overhang length. (**B**) Binding of replication fork vs. ssDNA overhangs. Binding assays were performed in triplicates and data were plotted as mean ± SD. Native EMSA of GRF:DNA binding without a fluorescent dye is shown in Supplementary Figure S4 and further data; e.g. K_D values and the remaining binding curves and raw fluorescence and anisotropies are shown in Supplementary Figure S5. The alternative fit with two-site model is shown Supplementary Figure S6.

reaction of the mouse NEI domain and the Ap site with $NaBH_3CN$ (57). We used several different DNA substrates, including DNA hairpins with ssDNA overhangs mimicking a simplified DNA replication fork with only one arm. Both of the DNA hairpin substrates were mirror images, with 6T long 3′- or 5′-overhangs. Despite the aforementioned preference of NEIL3 towards the Ap site before the 3′ overhang (Figure 3), we obtained well-diffracting crystals only for NEIL3:DNAhp with a 5′ overhang. The crystals diffracted to 2.28 Å resolution (PDB ID 7Z5A), and the structure was solved by molecular replacement using a mouse NEIL3 apo structure (PDB ID 3W0F) as a search model and refined

to good geometry and R factors (please see Supplementary Table S2 for more details) (52).

The structure of the NEI domain consists of two subdomains, NTD and CTD. NTD domain contains catalytic residues with the reactive amino group of the N-terminus followed by eight anti-parallel beta-sheets that form a sandwich flanked by a small pair of helices and a large loop that is only partially visible in the electron density, likely due to its flexibility. The protein is connected via a further pair of α-helices, with CTD containing four helices and a zinc-finger with two antiparallel β-sheets. The overall fold is not only very similar to the apo form but also to the fold of
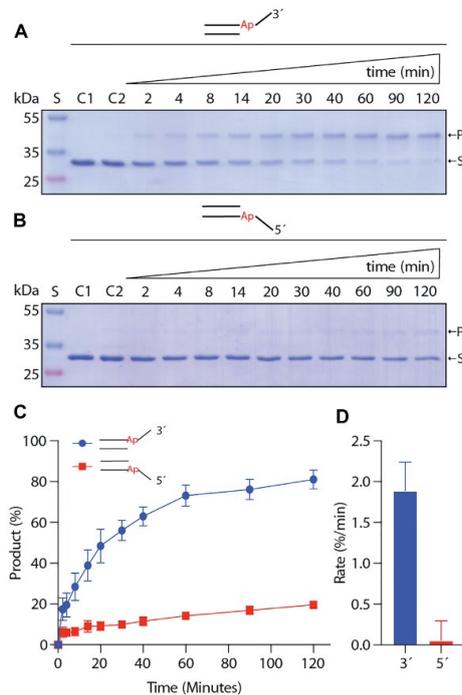
Figure 3. NEIL3 enzymatic assays with native Ap site within dsDNA with 3′- or 5′-overhangs. Enzymatic reactions of the mNEIL3 NEI domain with DNA with (**A**) 3′-overhangs (**B**) 5′-overhangs. Reactions were captured by the formation of the covalent intermediate by reducing the Schiff-base with $NaBH_3CN$ and resolved on 15% SDS-PAGE. (**C**) Gels bands corresponding to the substrate (S) and products (P) were quantified and plotted against reaction time. (**D**) Initial rates were calculated and plotted. Reactions were repeated in triplicates. The error is an SD (standard deviation).

the other members of the Nei/Fpg family (57). The orientation of NTD and CTD is identical to the published apo (unliganded) crystal structures of the mouse NEIL3 (52). This is in contrast with some Nei/Fpg enzymes that undergo conformational changes upon DNA binding (38). As previously reported, NTD and CTD are locked by a network of hydrogen and salt bridges between individual domains (Supplementary Figure S8E) (52). The lack of interdomain rearrangements and large interdomain interface suggests more interdomain rigidity in the NEIL3 glycosylase.

NEIL3 and the recognition of a trapped intermediate-like DNA hairpin with a 5′ overhang

The structural superimposition of apo and DNA:mNEIL3 structures of NEI domains revealed that DNA does not contribute to any significant conformational changes in the NEI domain (RMSD = 0.394 Å) (Supplementary Figure

S7) (58). Several loops on both sides of the DNA strand relocate in order to accommodate the substrate.

The trapped DNA molecule is recognised exclusively in the vicinity of the active site residue and further on towards the hairpin and its 3′ end. At this point, residues K82, H96, R94 and N193 are responsible for the interaction with the damaged part of the strand. Furthermore, the active site methionine M1 is covalently linked with the Ap site that is stabilized by the hydrogen bridge E3 and further anchored by M99 and R272 (Figure 4). In contrast, besides the hydrogen bridge with Y243, there is an apparent lack of specific interaction between the protein and the ssDNA backbone on the 5′ end from the damaged site (Supplementary Figure S8).

Structural aspects of NEIL3 preference for ssDNA

Overall, our data on the structure of the NEI domain with DNA has confirmed several predictions that were based on the apo structure (52). This work on the structure of mNEIL3 has suggested several differences between NEIL3 and other enzymes from Fpg/Nei family that our NEI:DNA structure has confirmed (52). There is a complete lack of contact between the complementary DNA strand and the enzyme. In addition, two acidic residues, E269 and D175, do not favour the recognition of the opposite strand of DNA (Supplementary Figures S7 and S8). Since, NEIL3 glycosylase is the Ap-ICL repairing glycosylase, the damaged oxidized base 'capping loop' (αF-β9/10 loop of Fpg/Nei enzymes) is completely missing, suggesting that the recognition and accommodation of the Ap-ICL and the entire associated DNA structures are carried out by different mechanisms. Interestingly, N-terminal methionine was involved in catalysis and not cleaved off, as it is for other members of the family (Figure 4 and Supplementary Figure S7).

NEIL3 and possible recognition of DNA replication fork intermediates

We conducted experiment-driven modelling to unravel the recognition of the replication fork structures by NEIL3 glycosylase. First, we took an AlphaFold (AF) generated model of the entire NEIL3 where GRFs are in contact with the NEI domain (Figure 5A). Then, using the AF model, we superimposed our structures of GRFs and NEI domains with DNA (Figure 5B). The structures matched relatively well to the AF model (RMSD (NEI) = 0.453 Å and RMSD (GRF1&2) = 1.980 Å). Interestingly, the orientation of GRFs and NEI is such that DNA from the NEI domain overlaps with the DNA of the GRF dimer in a shape letter Y, resembling the DNA replication fork (Figure 5B). We constructed a model of the DNA replication fork bound to NEIL3 glycosylase mid-repair. In this model, we used the interdomain arrangement from the AF and connected DNA strands from both the crystal structure of NEI:DNA and NMR-modelled structure GRF1&2:DNA. The hairpin turn in the dsDNA part of the model was maintained for clarity (Figure 5C, D).
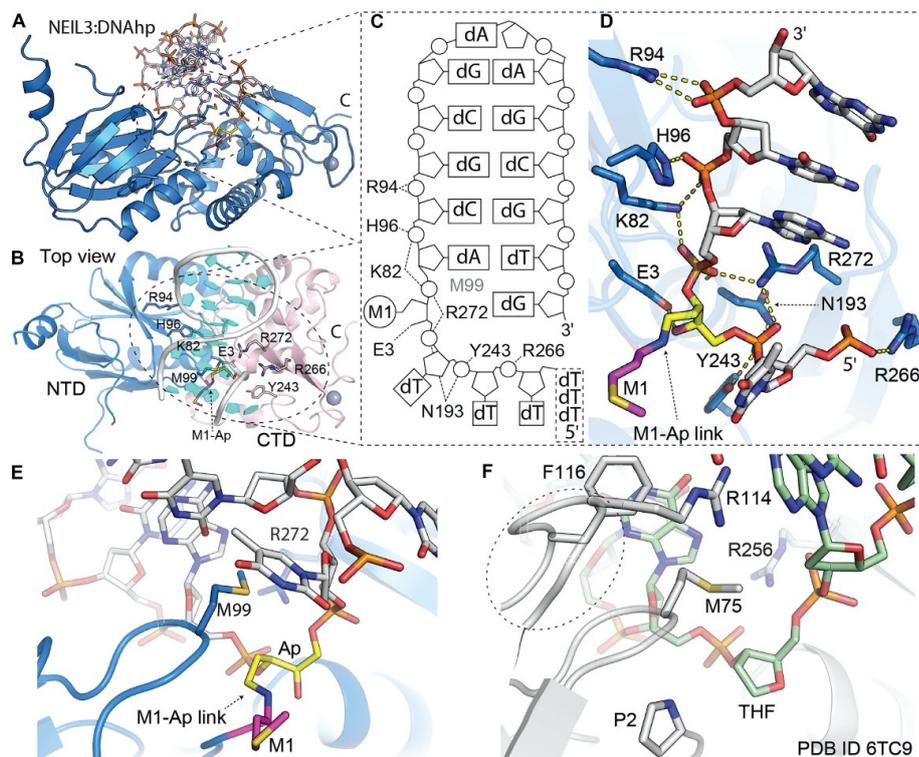
89

Figure 4. Crystal structure of trapped mouse NEIL3:ssDNAhp complex; DNA hairpin with 5′ overhang. (**A**) Overall structure of NEI glycosylase domain (light blue PDB ID 7Z5A) trapped in complex with DNA hairpin. (**B**) Top view on the NEIL3:DNA complex with highlighted residues involved in DNA interaction (sticks) N-terminal and C-terminal domains (NTD light blue and CTD in light pink). (**C**) Scheme of the interactions between DNA and NEI domain, M99 is intercalated between the Ap site and an orphan base. Structural representation of NEI residues directly involved in interaction with DNA. (**D**) Detail of the DNA binding pocket with reduced Shiff-base between methionine (M1) and Ap-site (M-Ap link). (**E, F**) A comparison of the active site of mouse NEIL3 glycosylase and bacterial fpg; fpg:dsDNA complex (PDB ID: 6TC9) with the Ap site analogue (THF), the typical residues for Nei/Fpg, here F116, R114, M75 inserted in the place of the damaged base. Two of these residues (R114&F116) are missing in the case of NEIL3 (38). For further comparison of mNEIL3 NEI domain and bacterial Fpg protein that undergoes a conformational change upon DNA binding the Supplementary Figure S9.

DISCUSSION

From GRF inhibition to a two-fork recognition mechanism

Using NMR spectroscopy, we obtained the structures of tandem GRF domains from mouse *Neil3* (Figure 1C). The work reporting the crystal structure of human GRF domains suggests some interdomain motion (Figure 1D) (35). On the other hand, our data indicate restricted interdomain movement between GRF1&2, suggesting a relative rigidity between these domains. The GRF dimer interface is fortified by salt and hydrogen bridge interactions. These interactions include residues R560, D549, and R529, interactions with mainchain atoms A548 with Q530, R560 with F552. The residues at the N- and C- termini of the GRF domains

are involved (E595 and S505, R514 and G597) (Supplementary Figure S9). Our NMR measurements do not support this behaviour in the case of the mouse protein homologue as for all ensembles for apo and DNA bound GRF dimer the structure is virtually identical. Moreover, our biochemical data indicate the ability of GRF to bind short replication forks, and the GRF dimer has an ideal arrangement to accommodate the branching point of the replication fork, with each domain binding one DNA strand. These data together suggest the possible role of GRFs in the binding of replication structures during the repair.

Recent work has demonstrated that GRF domains inhibit the enzymatic activity of the NEIL3 NEI domain (35). This observation might seem surprising, as other studies
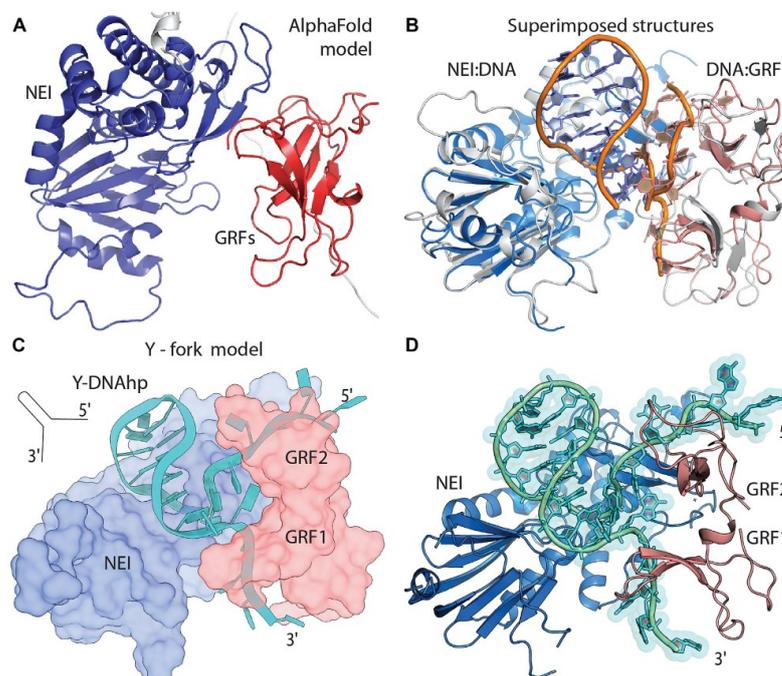
Figure 5. From the AlphaFold model and our NEI and GRFs DNA complexes to recognition of DNA replication fork. (**A**) AlphaFold (AF) model of NEI (blue) and GRF1&2 domains (red). (**B**) Superimposed crystal structure of NEI:hpDNA (light blue) and NMR model GRF1&2 (light red) with ssDNA on AF model (here white), DNA backbones (orange). (**C**) Schematics of an experimentally driven model where one replication DNA fork is recognised by NEI&GRFs based on AF interdomain positions. (**D**) cartoon representation of the model of Y-DNA:NEI&GRFs complex.

have shown that GRFs are known to stimulate the activity of the enzyme containing this domain (33,55). Competition of GRF and NEI for ssDNA may explain the observed decrease of the reaction rate catalysed by the NEI domain (35). This data could be explained as follows, both GRF1&2 and NEI domains efficiently bind Y forked substrates in their ssDNA parts, therefore they could simply be competing for the substrate of the NEIL3 enzyme. Therefore, the single Y-fork model scenario can explain the previously observed GRF inhibition of the NEI domain during the catalysis.

We predicted two different models for the role of GRF domains in Ap-ICL repair. Either GRF inhibits or regulates the enzymatic activity of the NEI domain, or GRF increases the selectivity of the NEIL3 enzyme towards structurally more complex substrates generated during the replication coupled repair of the Ap-ICL (19). Here, we propose a model that assumes that GRF1&2 bind a DNA replication fork at the interface with NEI, resulting in a Y-structured DNA replication fork model (Figure 5D). Two converging forks from each direction were observed during the efficient crosslink repair in *Xenopus* egg extracts (14,19,32). There-

fore, we suggest a two-fork model, with the mechanism of its recognition accomplished by NEIL3 (Figure 6).

The single-fork model and our NEI domain crystal structure both contain fork-like structures that are in an orientation that does not favour enzymatic catalysis (Figure 5). For efficient catalysis, the fork branching point or the 3′ ssDNA overhang mimicking the replication fork should be oriented in the opposite direction, away from the GRF domains, with the 3′ ssDNA branch of the fork located towards the DNA binding pocket and the residues K82, H96, and R94 (Figures 3 and 4) (56). If we suppose that the AlphaFold prediction of this GRF:NEI interdomain interaction is correct, the GRF would bind one fork to one end of the DNA, and the NEI domain would require a free 3′ ssDNA end for efficient catalysis. To fulfil the requirement of the NEI domain for ssDNA and to avoid competition for the substrate, the second fork must be present, forming a structure in the shape of the letter X (Figure 6). Both NEI and GRF domains bind the ssDNA part of the fork-like structures in a complementary manner. This is due to the preference of GRFs for 5′ ends and the preference of NEI for 3′ ends, while both bind replication forks. Together, bio-
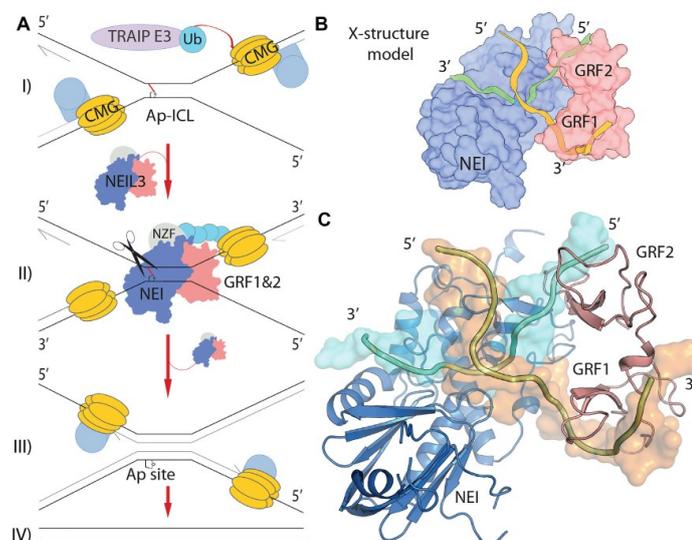
Figure 6. DNA X-structure of replication-coupled DNA repair of the Ap-ICL. (**A**) A model of replication coupled repair of the Ap-ICL (32). I) Two replication forks stall upon the crosslink. The CMG helicase (yellow) is ubiquitylated by TRAIP1 (light purple). Ubiquitin chains recruit NEIL3 (NEI, GRFs, NZF; blue, red, slate) II) NEIL3 recognition of the double fork, the DNA X-structure at Ap-ICL. III) The Ap-ICL has been unhooked, followed by further steps of the repair. IV) Finally, repaired daughter strands (19,32). (**B**) Schematics of design of the model. (**C**) Final model of NEIL3 bound to the X-structure, experimentally driven model of stalled replication fork on the Ap-ICL recognised by NEI (blue) and GRF1&2 (red) domains of NEIL3 glycosylase. Damaged DNA strand containing Ap-site leading to the crosslink (cyan), undamaged strand (orange)

chemical data and predictions indicate that GRF recognizes one fork and the NEI domain recognizes the other fork of the X-structure (Figure 6) (56). While GRFs might bind one or both arms of the fork. An X-structure is commonly drawn in repair models as a prediction of the repair centre, as it was initially based on an electron micrograph from seminal work on ICL repair (14). Additionally, several seminal publications from J. C. Walter's laboratory proposed this model of two stalled replication forks (15,19). Overall, the two-fork model proposed here with NEIL3 glycosylase resembles an X-structure, one fork is recognized by NEI, and the other fork is recognized by GRF. The orientation is such that the Ap site is located in the NEI's active site pocket (Figure 6). Our structural and biochemical data strongly support that two forks are required for the efficient Ap-ICL repair by NEIL3 glycosylase. Although many models are possible for binding of NEIL3, our data is consistent with a simple model whereby NEIL3 can engage a double-fork structure which might occur with converging replication forks at the ICL. Additional studies are necessary to evaluate it.

X-structure flexibility allows Ap-ICL flipping-out mechanism

If an X-structure is present, the rate of the repair will not be impeded by competition for the fork by the interaction with GRF. Instead, both NEI and GRFs would bind one of the forks in their preferred orientation, with the Ap site in

the active site pocket. This would result in efficient crosslink repair.

However, the general mechanism of the Fpg/Nei family of enzymes involves the damaged base flipping outwards into the active site pocket (59). This movement allows for a nucleophilic attack of the *N*-glycosidic bond of the lesion. Such an action requires dramatic conformational changes within the duplex (60). No flip-out mechanism of the lesion seems possible in the case where dsDNA is crosslinked to another strand. It Is more likely that the entire DNA chain is rotated in the active site pocket.

The dsDNA is relatively rigid on its own, and the addition of an interstrand crosslink would restrict yet another degree of freedom. In the case of an X-structure, all four ssDNA arms could move relatively freely. We predict that once the substrate is recognised by the enzyme, the X-structure arrangement would allow one of the DNA strands to rotate with the crosslink in a 'flip-out-like' mechanism, positioning the *N*-glycosidic bond of the Ap-ICL towards the active site residue. This then allows for a nucleophilic attack, the formation of the Shiff-base, and unhooking of the crosslink, therefore liberating one strand from the other. Then the further steps of Ap-ICL repair can continue.

DATA AVAILABILITY

The structural data generated for this study have been deposited into the Protein Data Bank under the PDB codes

7OMK for GRF, and 7Z5A for NEI glycosylase domains of NEIL3.

SUPPLEMENTARY DATA

Supplementary Data are available at NAR Online.

ACKNOWLEDGEMENTS

We would like to thank Sebastian Zoll for his invaluable advice, and Tamara Jenkins for proofreading the manuscript.

REFERENCES

1. Zhang,J. and Walter,J.C. (2014) Mechanism and regulation of incisions during DNA interstrand cross-link repair. *DNA Repair (Amst.)*, **19**, 135–142.
2. Langevin,F., Crossan,G.P., Rosado,I.V., Arends,M.J. and Patel,K.J. (2011) Fancd2 counteracts the toxic effects of naturally produced aldehydes in mice. *Nature*, **475**, 53–59.
3. Aqeel,A., Zafar,J., Ehsan,N., Qurat-Ul-Ain, Tariq,M. and Hannan,A. (2021) Interstrand crosslink repair: new horizons of DNA damage repair. In: Behzadi,P, (ed). *DNA*. IntechOpen, Rijeka.
4. Coste,F., Malinge,J.M., Serre,L., Shepard,W., Roth,M., Leng,M. and Zelwer,C. (1999) Crystal structure of a double-stranded DNA containing a cisplatin interstrand cross-link at 1.63 Å resolution: hydration at the platinated site. *Nucleic Acids Res.*, **27**, 1837–1846.
5. Kellum,A.H., Qiu,D.Y., Voehler,M.W., Martin,W., Gates,K.S. and Stone,M.P. (2021) Structure of a stable interstrand DNA cross-link involving a β- N-glycosyl linkage between an N6-dA amino group and an abasic site. *Biochemistry*, **60**, 41–52.
6. Huang,H. and Hopkins,P.B. (1993) DNA interstrand cross-linking by formaldehyde: nucleotide sequence preference and covalent structure of the predominant cross-link formed in synthetic oligonucleotides. *J. Am. Chem. Soc.*, **115**, 9402–9408.
7. Cho,Y.J., Kozekov,I.D., Harris,T.M., Rizzo,C.J. and Stone,M.P. (2001) Stereochemistry modulates the stability of reduced interstrand cross-links arising from R-and. *Chem. Res. Toxicol.*, **14**, 2608–2621.
8. Rink,S.M., Solomon,M.S., Taylor,M.J., Rajur,S.B., McLaughlin,L.W. and Hopkins,P.B. (1993) Covalent structure of a nitrogen mustard-induced DNA interstrand cross-link: an N7-to-N7 linkage of deoxyguanosine residues at the duplex sequence 5'-d(GNC). *J. Am. Chem. Soc.*, **115**, 2551–2557.
9. Dutta,S., Chowdhury,G. and Gates,K.S. (2007) Interstrand cross-links generated by abasic sites in duplex DNA. *J. Am. Chem. Soc.*, **129**, 1852–1853.
10. Johnson,K.M., Price,N.E., Wang,J., Fekry,M.I., Dutta,S., Seiner,D.R., Wang,Y. and Gates,K.S. (2013) On the formation and properties of interstrand DNA-DNA cross-links forged by reaction of an abasic site with the opposing guanine residue of 5'-CAp sequences in duplex DNA. *J. Am. Chem. Soc.*, **135**, 1015–1025.
11. Price,N.E., Johnson,K.M., Wang,J., Fekry,M.I., Wang,Y. and Gates,K.S. (2014) Interstrand DNA–DNA cross-link formation between adenine residues and abasic sites in duplex DNA. *J. Am. Chem. Soc.*, **136**, 3483–3490.
12. Huskova,A., Landova,B., Boura,E. and Silhan,J. (2022) The rate of formation and stability of abasic site interstrand crosslinks in the DNA duplex. *DNA Repair (Amst.)*, **113**, 103300.
13. Garaycoechea,J.I., Crossan,G.P., Langevin,F., Daly,M., Arends,M.J. and Patel,K.J. (2012) Genotoxic consequences of endogenous aldehydes on mouse haematopoietic stem cell function. *Nature*, **489**, 571–575.
14. Räschle,M., Knipscheer,P., Enoiu,M., Angelov,T., Sun,J., Griffith,J.D., Ellenberger,T.E., Schärer,O.D. and Walter,J.C. (2008) Mechanism of replication-coupled DNA interstrand crosslink repair. *Cell*, **134**, 969–980.
15. Knipscheer,P., Räschle,M., Smogorzewska,A., Enoiu,M., Ho,T.V., Schärer,O.D., Elledge,S.J. and Walter,J.C. (2009) The fanconi anemia pathway promotes replication-dependent DNA interstrand cross-link repair. *Science*, **326**, 1698–1701.
16. Auerbach,A.D. and Wolman,S.R. (1976) Susceptibility of fanconi's anaemia fibroblasts to chromosome damage by carcinogens. *Nature*, **261**, 494–496.
17. Kim,H. and D'Andrea,A.D. (2012) Regulation of DNA cross-link repair by the fanconi anemia/BRCA pathway. *Genes Dev.*, **26**, 1393–1408.
18. Sasaki,M.S. and Tonomura,A. (1973) A high susceptibility of fanconi's anemia to chromosome breakage by DNA cross-linking agents. *Cancer Res.*, **33**, 1829–1836.
19. Semlow,D.R., Zhang,J., Budzowska,M., Drohat,A.C. and Walter,J.C. (2016) Replication-Dependent unhooking of DNA interstrand cross-links by the NEIL3 glycosylase. *Cell*, **167**, 498–511.
20. Takao,M., Oohata,Y., Kitadokoro,K., Kobayashi,K., Iwai,S., Yasui,A., Yonei,S. and Zhang,Q.M. (2009) Human Nei-like protein NEIL3 has AP lyase activity specific for single-stranded DNA and confers oxidative stress resistance in escherichia coli mutant. *Genes Cells*, **14**, 261–270.
21. Liu,M., Bandaru,V., Bond,J.P., Jaruga,P., Zhao,X., Christov,P.P., Burrows,C.J., Rizzo,C.J., Dizdaroglu,M. and Wallace,S.S. (2010) The mouse ortholog of NEIL3 is a functional DNA glycosylase in vitro and in vivo. *Proc. Natl. Acad. Sci. U.S.A.*, **107**, 4925–4930.
22. Wallace,S.S. (2014) Base excision repair: a critical player in many games. *DNA Repair (Amst.)*, **19**, 14–26.
23. Bandaru,V., Sunkara,S., Wallace,S.S. and Bond,J.P. (2002) A novel human DNA glycosylase that removes oxidative DNA damage and is homologous to escherichia coli endonuclease VIII. *DNA Repair (Amst.)*, **1**, 517–529.
24. Hazra,T.K., Kow,Y.W., Hatahet,Z., Imhoff,B., Boldogh,I., Mokkapati,S.K., Mitra,S. and Izumi,T. (2002) Identification and characterization of a novel human DNA glycosylase for repair of cytosine-derived lesions. *J. Biol. Chem.*, **277**, 30417–30420.
25. Morland,I., Rolseth,V., Luna,L., Rognes,T., Bjørås,M. and Seeberg,E. (2002) Human DNA glycosylases of the bacterial Fpg/MutM superfamily: an alternative pathway for the repair of 8-oxoguanine and other oxidation products in DNA. *Nucleic Acids Res.*, **30**, 4926–4936.
26. Takao,M., Kanno,S., Shiromoto,T., Hasegawa,R., Ide,H., Ikeda,S., Sarker,A.H., Seki,S., Xing,J.Z., Le,X.C. *et al.* (2002) Novel nuclear and mitochondrial glycosylases revealed by disruption of the mouse nth1 gene encoding an endonuclease III homolog for repair of thymine glycols. *EMBO J.*, **21**, 3486–3493.
27. Bhagwat,M. and Gerlt,J. a (1996) 3'- and 5'-strand cleavage reactions catalyzed by the fpg protein from escherichia coli occur via successive beta- and delta-elimination mechanisms, respectively. *Biochemistry*, **35**, 659–665.
28. Bruner,S.D., Norman,D.P. and Verdine,G.L. (2000) Structural basis for recognition and repair of the endogenous mutagen 8-oxoguanine in DNA. *Nature*, **403**, 859–866.
29. Krokan,H.E. and Bjoras,M. (2013) Chapter 06: base excision repair. *Cold Spring Harb. Perspect. Biol.*, **5**, a012583.
30. Silhan,J., Zhao,Q., Boura,E., Thomson,H., Förster,A., Tang,C.M., Freemont,P.S. and Baldwin,G.S. (2018) Structural basis for recognition and repair of the 3'-phosphate by NExo, a base excision DNA repair nuclease from neisseria meningitidis. *Nucleic Acids Res.*, **46**, 11980–11989.
31. Zhou,J., Liu,M., Fleming,A.M., Burrows,C.J. and Wallace,S.S. (2013) Neil3 and NEIL1 DNA glycosylases remove oxidative damages from quadruplex DNA and exhibit preferences for lesions in the telomeric sequence context. *J. Biol. Chem.*, **288**, 27263–27272.
32. Wu,R.A., Semlow,D.R., Kamimae-Lanning,A.N., Kochenova,O.V, Chistol,G., Hodskinson,M.R.G., Amunugama,R., Sparks,J.L.,

93

Wang,M., Deng,L. *et al.* (2019) TRAIP is a master regulator of DNA interstrand crosslink repair. *Nature*, **567**, 267–272.

33. Wallace,B.D., Berman,Z., Mueller,G.A., Lin,Y., Chang,T., Andres,S.N., Wojtaszek,J.L., DeRose,E.F., Appel,C.D., London,R.E. *et al.* (2017) APE2 Zf-GRF facilitates 3′-5′ resection of DNA damage following oxidative stress. *Proc. Natl Acad. Sci. U.S.A.*, **114**, 304–309.

34. Ha,A., Lin,Y. and Yan.S. (2020) A non-canonical role for the DNA glycosylase NEIL3 in suppressing APE1 endonuclease-mediated ssDNA damage. *J. Biol. Chem.*, **295**, 14222–14235.

35. Rodriguez,A.A., Wojtaszek,J.L., Greer,B.H., Haldar,T., Gates,K.S., Williams,R.S. and Eichman,B.F. (2020) An autoinhibitory role for the GRF zinc finger domain of DNA glycosylase NEIL3. *J. Biol. Chem.*, **295**, 15566–15575.

36. Gibson,D.G., Young,L., Chuang,R.-Y., Venter,J.C., Hutchison,C.A. and Smith,H.O. (2009) Enzymatic assembly of DNA molecules up to several hundred kilobases. *Nat. Methods*, **6**, 343–345.

37. Cihlova,B., Huskova,A., Böserle,J., Nencka,R., Boura,E. and Silhan,J. (2021) High-throughput fluorescent assay for inhibitor screening of proteases from rna viruses. *Molecules*, **26**, 3792.

38. Landova,B. and Silhan,J. (2020) Conformational changes of DNA repair glycosylase MutM triggered by DNA binding. *FEBS Lett.*, **594**, 3032–3044.

39. Renshaw,P.S., Lightbody,K.L., Veverka,V., Muskett,F.W., Kelly,G., Frenkiel,T.A., Gordon,S.V., Hewinson,R.G., Burke,B., Norman,J. *et al.* (2005) Structure and function of the complex formed by the tuberculosis virulence factors CFP-10 and ESAT-6. *EMBO J.*, **24**, 2491–2498.

40. Veverka,V., Lennie,G., Crabbe,T., Bird,I., Taylor,R.J. and Carr,M.D. (2006) NMR assignment of the mTOR domain responsible for rapamycin binding. *J. Biomol. NMR*, **36**, 3.

41. Herrmann,T., Güntert,P. and Wüthrich,K. (2002) Protein NMR structure determination with automated NOE assignment using the new software CANDID and the torsion angle dynamics algorithm DYANA. *J. Mol. Biol.*, **319**, 209–227.

42. Shen,Y., Delaglio,F., Cornilescu,G. and Bax,A. (2009) TALOS+: a hybrid method for predicting protein backbone torsion angles from NMR chemical shifts. *J. Biomol. NMR*, **44**, 213–223.

43. Harjes,E., Harjes,S., Wohlgemuth,S., Müller,K.H., Krieger,E., Herrmann,C. and Bayer,P. (2006) GTP-Ras disrupts the intramolecular complex of C1 and RA domains of nore1. *Structure*, **14**, 881–888.

44. Ferrage,F., Reichel,A., Battacharya,S., Cowburn,D. and Ghose,R. (2010) On the measurement of 15N-{1H} nuclear overhauser effects. 2. Effects of the saturation scheme and water signal suppression. *J. Magn. Reson.*, **207**, 294–303.

45. Ferrage,F. (2012) Protein dynamics by 15N nuclear magnetic relaxation. In: Shekhtman,A. and Burz,D.S. (eds). *Protein NMR Techniques*. Humana Press, Totowa, NJ, pp. 141–163.

46. Veverka,V., Crabbe,T., Bird,I., Lennie,G., Muskett,F.W., Taylor,R.J. and Carr,M.D. (2008) Structural characterization of the interaction of mTOR with phosphatidic acid and a novel class of inhibitor:

47. Harper,C.C., Berg,J.M. and Gould,S.J. (2003) PEX5 binds the PTS1 independently of hsp70 and the peroxin PEX12. *J. Biol. Chem.*, **278**, 7897–7901.

48. Obsilova,V., Herman,P., Vecer,J., Sulc,M., Teisinger,J. and Obsil,T. (2004) 14-3-3ζ C-terminal stretch changes its conformation upon ligand binding and phosphorylation at thr232. *J. Biol. Chem.*, **279**, 4531–4540.

49. Silhan,J., Obsilova,V., Vecer,J., Herman,P., Sulc,M., Teisinger,J. and Obsil,T. (2004) 14-3-3 protein C-terminal stretch occupies ligand binding groove and is displaced by phosphopeptide binding. *J. Biol. Chem.*, **279**, 49113–49119.

50. Kabsch,W. (2010) xds. *Acta Crystallogr. Sect. D Biol. Crystallogr.*, **66**, 125–132.

51. Evans,P.R. and Murshudov,G.N. (2013) How good are my data and what is the resolution? *Acta Crystallogr. Sect D Biol. Crystallogr.*, **69**, 1204–1214.

52. Liu,M., Imamura,K., Averill,A.M., Wallace,S.S. and Doublié,S. (2013) Structural characterization of a mouse ortholog of human NEIL3 with a marked preference for single-stranded DNA. *Structure*, **21**, 247–256.

53. Emsley,P., Lohkamp,B., Scott,W.G. and Cowtan,K. (2010) Features and development of coot. *Acta Crystallogr. Sect D Biol. Crystallogr.*, **66**, 486–501.

54. Liebschner,D., Afonine,P.V., Baker,M.L., Bunkoczi,G., Chen,V.B., Croll,T.I., Hintze,B., Hung,L.W., Jain,S., McCoy,A.J. *et al.* (2019) Macromolecular structure determination using X-rays, neutrons and electrons: recent developments in phenix. *Acta Crystallogr. Sect. D Struct. Biol.*, **75**, 861–877.

55. Tan,K., Zhou,Q., Cheng,B., Zhang,Z., Joachimiak,A. and Tse-Dinh,Y.C. (2015) Structural basis for suppression of hypernegative DNA supercoiling by *E. coli* topoisomerase I. *Nucleic Acids Res.*, **43**, 11031–11046.

56. Imani Nejad,M., Housh,K., Rodriguez,A.A., Haldar,T., Kathe,S., Wallace,S.S., Eichman,B.F. and Gates,K.S. (2020) Unhooking of an interstrand cross-link at DNA fork structures by the DNA glycosylase NEIL3. *DNA Repair (Amst.)*, **86**, 102752.

57. Gilboa,R., Zharkov,D.O., Golan,G., Fernandes,A.S., Gerchman,S.E., Matz,E., Kycia,J.H., Grollman,A.P. and Shoham,G. (2002) Structure of formamidopyrimidine-DNA glycosylase covalently complexed to DNA. *J. Biol. Chem.*, **277**, 19811–19816.

58. Liu,M., Doublié,S. and Wallace,S.S. (2013) Neil3, the final frontier for the DNA glycosylases that recognize oxidative damage. *Mutat. Res. - Fundam. Mol. Mech. Mutagen.*, **743–744**, 4–11.

59. Sugahara,M., Mikawa,T., Kumasaka,T., Yamamoto,M., Kato,R., Fukuyama,K., Inoue,Y. and Kuramitsu,S. (2000) Crystal structure of a repair enzyme of oxidatively damaged DNA, MutM (Fpg), from an extreme thermophile, thermus thermophilus HB8. *EMBO J.*, **19**, 3857–3869.

compelling evidence for a central role of the FRB domain in small molecule-mediated regulation of mTOR. *Oncogene*, **27**, 585–595.